

All-Photonic Architecture for Scalable Quantum Computing with Greenberger-Horne-Zeilinger States

Srikrishna Omkar^{1,*}, Seok-Hyung Lee,¹ Yong Siah Teo¹, Seung-Woo Lee,² and Hyunseok Jeong^{1,†}

¹*Department of Physics and Astronomy, Seoul National University, Seoul 08826, Korea*

²*Center for Quantum Information, Korea Institute of Science and Technology, Seoul 02792, Korea*

 (Received 30 September 2021; revised 28 February 2022; accepted 21 June 2022; published 18 July 2022)

Linear optical quantum computing is beset by the lack of deterministic entangling operations besides photon loss. Motivated by advancements at the experimental front in deterministic generation of various kinds of multiphoton entangled states, we propose an architecture for linear-optical quantum computing that harnesses the availability of three-photon Greenberger-Horne-Zeilinger (GHZ) states. Our architecture and its subvariants use polarized photons in GHZ states, polarization beam splitters, delay lines, optical switches, and on-off detectors. We concatenate the topological quantum error-correction code with three-qubit repetition codes and estimate that our architecture can tolerate a remarkably high photon-loss rate of 11.5%; this makes a drastic change that is at least an order higher than those of known proposals. Furthermore, considering three-photon GHZ states as resources, we estimate the resource overheads to perform gate operations with an accuracy of 10^{-6} (10^{-15}) to be 2.07×10^6 (5.03×10^7). Compared to other all-photonic schemes, our architecture is also resource efficient. In addition, the resource overhead can be even further improved if larger GHZ states are available. Given its striking enhancement in the photon-loss threshold and the recent progress in generating multiphoton entanglement, our scheme moves scalable photonic quantum computing a step closer to reality.

DOI: [10.1103/PRXQuantum.3.030309](https://doi.org/10.1103/PRXQuantum.3.030309)

I. INTRODUCTION

Out of the many physical platforms available for quantum computing, optical platforms facilitate quicker gate operations compared to the decoherence time, fast readouts, and efficient qubit transfer [1,2]. These features make them one of the strongest contenders for realizing scalable quantum computing. Linear optical quantum computing [1,3,4] uses only beam splitters, phase shifters, and photon detectors to process the quantum information encoded in light. Besides this apparent simplicity, the ability to operate at room temperature makes this approach attractive. Measurement-based quantum computing [5] is particularly suitable for optical platforms [6] in terms of practical implementation. In this approach, we first generate a particular class of multiqubit entangled states, known as cluster states, and single-qubit measurements are then performed on these states to realize a universal set of gate

operations. In optical platforms, linear optical elements are sufficient for implementing the entangling operations for the generation of cluster states as well as single-qubit measurements.

However, one major shortcoming that besets linear optical quantum computing is the fact that a *direct* Bell-state measurement (BSM), which is an entangling operation used to form a larger entangled state from smaller ones, is not deterministic [2,7]. Adding to the shortcoming, photon loss is ubiquitous in all optical platforms and specifically in integrated optics [8], which not only causes optical qubit states to leak out of the computational basis, but also introduces dephasing or depolarizing noise into qubits, gate operations, and readouts (measurements). Thus, the bare-bone measurement-based quantum-computing scheme in Ref. [5] is not tolerant against the aforementioned practical issues, and additional enhancements are necessary to ensure its successful execution in real experiments. To overcome indeterminism of BSM and quantum noise, we need fault-tolerant architectures that employ quantum error correction (QEC) [9,10]. With QEC, it is possible to achieve scalable linear optical quantum computing using lossy optical components provided the photon-loss level is below a certain threshold. This threshold value is dependent on the QEC codes and noise model considered in the fault-tolerant architecture [11–13].

*omkar.shrm@gmail.com

†h.jeong37@gmail.com

Published by the American Physical Society under the terms of the [Creative Commons Attribution 4.0 International](https://creativecommons.org/licenses/by/4.0/) license. Further distribution of this work must maintain attribution to the author(s) and the published article's title, journal citation, and DOI.

Various kinds of linear-optical platforms have been proposed for quantum computing depending on the nature of variables used for encoding quantum information. Discrete-variable (DV) platforms manipulate level-structure properties of photons like polarization to encode quantum states. A BSM on DV qubits using linear optics is probabilistic with a success rate of 50% without additional resources [7,14]. Fault-tolerant architectures for linear optical quantum computing in Refs. [6,13,15–18] overcome indeterminism of entangling operations by the *repeat-until-success* strategy. However, if we wish to carry out, say m simultaneous and identical entangling operations successfully, the average resource overhead is $O(1/p_s^m)$, which will result in an increase in overhead by a factor of $O(\Delta^m)$ that is exponential in m when the success rate p_s of each entangling operation decreases by a factor of Δ [15]. In our protocol, which we detail in Sec. II, the strategy with low success rates of entangling operations is used only at a certain stage unlike other mentioned architectures. This makes our protocol competitive in terms of resource overheads. Furthermore, because of such probabilistic entangling operations, these schemes would require *optical switches* to pass the successfully entangled states to the next step, which is known to contribute significant photon loss [19]. Alternatively, continuous-variable (CV) platforms that employ coherent states described by a continuous parameter (amplitude) [20–23] offer BSMs that can be nearly deterministic [24]. Here, the success rate of a BSM grows with the coherent-state amplitude. The corresponding architectures for linear optical quantum computing require lower resource overheads, but are sensitive to photon loss and can only tolerate smaller thresholds [22]. Also, there has been significant developments in using optical Gottesman-Kitaev-Preskill states for fault-tolerant quantum computing [25,26]. These schemes need very large squeezing strengths (>10 dB) to implement gates with high precision.

Recently, efforts have been made to combine the DV and CV approaches for quantum computing [27–31]. It was demonstrated that, by using optical *hybrid* qubits, which are entangled states in the DV and CV domains, near-deterministic entangling operations can be implemented [27,28]. Moreover, many shortcomings faced individually by CV and DV qubit-based schemes are overcome. Importantly, quantum computing with hybrid qubits reduces resource overheads and also improves the photon-loss tolerance [27–29]. By increasing the amplitude of the CV part, incurred resources can also be reduced. However, if the coherent amplitude of hybrid qubits is too large, the dephasing noise level in the presence of photon loss will also be commensurately too high [32]. Omkar *et al.* [29] also supported the logic that quantum computing on a special cluster state known as a Raussendorf-Harrington-Goyal (RHG) lattice [33,34] built with only DV qubits could tolerate higher photon loss, albeit at higher resource

costs. Larger cluster states like the RHG lattice are built by performing BSMs on smaller entangled states.

Besides probabilistic BSMs and photon loss, practical implementation of linear optical quantum computing is greatly hindered by indeterministic generation of multiphoton entangled states, such as the Greenberger-Horne-Zeilinger (GHZ) and cluster states. There are theoretical proposals for on-demand generations of such multiphoton entangled states [35,36]. For instance, various multiphoton entangled states can be generated by coupling a multilevel ancillary system to a two-level photon-emitting source and performing sequential unitary operation on both the ancillary system and source [35]. Here, the type of entangled states generated depends on the chosen unitary operation. In the experimental work [37], both the ancillary system and photon source are transmons, and are coupled *via* a flux-tunable superconducting quantum interference device. Furthermore, by interacting the single-photon sources, such as quantum dots, with spin-1/2 states, the sources can be made to emit multiphoton entangled states [36]. Recent experimental realizations [38,39] alternatively make use of entanglement between the electron spin and polarization of photons emitted from optical excitations. An interesting point is that experimentally realized three-photon and four-photon GHZ states respectively possess fidelities 0.9 and 0.82 [37]. We can also observe that as the number of photons in the GHZ state increases, the fidelity drops.

Motivated by state-of-the-art techniques in deterministic generation of multiphoton entangled states, in this work we propose a *multi-photon-qubit-based topological quantum computing* (MTQC) protocol that uses multiphoton GHZ polarization states from deterministic sources to build a RHG lattice. Furthermore, we demonstrate that our protocol provides an exceptionally high tolerance against photon loss that reaches 11.5%. Considering GHZ states as the raw ingredients, we also show that the protocol is more resource efficient than all known [13,17,22,27,40–42] nonhybrid qubit-based schemes. We further encode each qubit of the RHG lattice with a multiqubit repetition code [9]—a concatenation of two QEC codes—to improve the photon-loss tolerance. Another salient and practically favorable feature of our protocol is that it requires only on-off detectors, unlike Ref. [18] that demands detectors that can resolve photon numbers and are thus more difficult to implement with competitive accuracy. Also, photon-number-resolving nano-wire-based [43] and transition-edge-based [44] detectors cannot operate at room temperatures. However, on-off detectors can operate at room temperatures [45], which allows our MTQC protocol to pave the way for scalable all-photonic quantum computing.

The rest of the article is organized as follows. In Sec. II, we describe our MTQC protocol in detail. Next, in Sec. III, we discuss the noise model we consider throughout the work. Section IV touches on the employment of

concatenated QEC methods and their effects on further raising the threshold photon-loss rate that can be tolerated with our all-photon architecture, whereas the numerical simulation procedure of QEC is separately outlined in Appendix A. In Sec. V, we present our results on the photon-loss thresholds, and the details concerning resource estimation, specifically the average number of three-qubit GHZ states consumed, are provided in Sec. VI. In Sec. VII, we compare the results of our MTQC protocol with those of other linear optical quantum computing schemes. Finally, some pertinent discussion and conclusions are presented in Sec. IX.

II. PROTOCOL

The primary aim of MTQC is to build a RHG lattice for fault-tolerant quantum computing using multiphoton GHZ polarization states from deterministic sources and processing them with passive linear-optical elements like polarizing beam splitters, phase shifters, optical delay lines, optical switches, and on-off detectors. To begin, multiphoton GHZ states are entangled by BSMs in an efficient manner to form two kinds of *resource states*. We point out that, like other DV protocols, the repeat-until-success strategy with low-success-rate entangling operations is employed only at this stage to generate these resource states. After which, we perform a *collective BSM* [41] on multiphoton resource states, which is a near-deterministic entangling operation.

The collective BSM (described in Sec. II A) is a crucial ingredient of our protocol. This is because the near-deterministic entangling operation requires only on-off detectors to boost its success rate of entangling arbitrarily close to 100%. This is unlike some other BSMs [46,47] that demand photon-number-resolving detectors that can distinguish up to four photons to boost the success rate to 75%, and the ability to resolve higher photon numbers is essential for further enhancements. Another salient feature of the collective BSM is that it needs no optical switching to entangle two optical qubits like the other DV protocols when using the repeat-until-success strategy. These features make MTQC practically more attractive. It is also important to note that, once we start using collective BSMs in our protocol, the repeat-until-success strategy, even if employed, will not drastically increase resource overheads as the success rate of a collective BSM is very high. This makes our protocol competitive in terms of resource overheads.

The RHG lattice built using BSMs with a boosted success rate of 75% still cannot support fault-tolerant quantum computing as the failure rate must be less than 14.5% [48]. To overcome this shortfall, there exists a proposal to purify the RHG lattice [49] by which the effective failure rate of BSMs can be brought down to 7% from 25%. While the purified RHG lattice can support fault-tolerant quantum computing, this approach has the disadvantage of reducing

the effective size of the RHG lattice that will contribute to a large resource overhead. Also, in this situation the RHG lattice is less robust against dephasing errors. There was also an attempt to build the lattices with CV-based qubits in Ref. [23]. But this demands average photon numbers of CV qubits over 100 to build a RHG lattice that is of a sufficiently high fidelity for fault-tolerant computation. Such high average photon numbers are not achievable and lattices built under practical values [50] (average photon number of 2) are far from fault tolerant. Recently, there has been progress in the generation of two-dimensional CV cluster states without BSM [51,52]. Another proposal [18] aimed to build RHG lattices using BSMs with a boosted success rate of 75% (or higher) by adding single photons or Bell pairs and employing photon-number-resolving detectors. Here, the 14.5% failure-rate mark was overcome by the repeat-until-success strategy to create entanglement between qubits similar to Ref. [13]. Involvement of *tree clusters* [53,54] render the scheme fault tolerant against BSM failure, but this comes at the cost of feed-forward measurements. Depending on the failure or success of BSM, remaining qubits of the tree cluster are measured in an appropriate basis [18]. These feed-forward operations form the bottleneck in linear optical quantum computing.

The state $|\mathcal{C}_L\rangle$ of a RHG lattice is a unique three-dimensional cluster state [34] where qubits are entangled to their nearest neighbors represented by the edges of the RHG lattice. In general, a cluster state $|\mathcal{C}\rangle$ over a collection of qubits \mathcal{C} is a state stabilized by the operators $X_a \otimes_{b \in \text{nh}(a)} Z_b$, where $a, b \in \mathcal{C}$, Z_i and X_i are the Pauli operators on the i th qubit, and $\text{nh}(a)$ denotes the adjacent neighborhood of qubit $a \in \mathcal{C}$:

$$|\mathcal{C}\rangle = \prod_{\substack{a \in \mathcal{C} \\ a < b \in \text{nh}(a)}} CZ_{a,b} \bigotimes_{a' \in \mathcal{C}} |+\rangle_{a'}. \quad (1)$$

Here $|\pm\rangle = (|0\rangle \pm |1\rangle)/\sqrt{2}$ are eigenkets of X , while $|0\rangle, |1\rangle$ are those of Z . The controlled- Z unitary gate $CZ_{a,b}$, which is an entangling operation, applies Z on the target qubit b if the source qubit a is in state $|1\rangle$. The successful action of $CZ_{a,b}$ on the lattice qubits on sites a and b is represented by an edge in the lattice. The state $|\mathcal{C}_L\rangle$ is currently the best available choice, to the best of our knowledge, to make a linear-optical platform fault tolerant; it can tolerate qubit loss [55,56], probabilistic entangling operations [15,48], dephasing, and depolarizing noises [33,34,57], all of which are peculiar to the platform. Furthermore, QEC and gate operations on $|\mathcal{C}_L\rangle$ are topological in nature and thus offer the highest fault tolerance in the platforms where interactions are restricted to those of the nearest neighbors [58].

In MTQC, the logical basis for an l -photon qubit is

$$|0_l\rangle \equiv |H\rangle^{\otimes l}, \quad |1_l\rangle \equiv |V\rangle^{\otimes l}. \quad (2)$$

where $|H\rangle$, $|V\rangle$ are the discrete orthonormal polarizations, and are eigenkets of the Z Pauli operator. An r -photon GHZ ket has the form $|\text{GHZ}_r\rangle \propto |H\rangle^{\otimes r} + |V\rangle^{\otimes r}$ (up to normalization). Once there is a continuous and reliable supply of $|\text{GHZ}_r\rangle$ from deterministic sources, the following prescription forms the stages of our protocol to create $|\mathcal{C}_L\rangle$ and perform topological fault-tolerant quantum computing on it.

1. The foremost step is to create multiphoton three-qubit resource states using $|\text{GHZ}_r\rangle$ and BSMs.
2. Near-deterministic collective BSMs are performed on these resource states to form *star cluster states*.
3. The star clusters then undergo collective BSM to form layers of $|\mathcal{C}_L\rangle$.
4. Finally, the qubits are measured layer by layer in a suitable basis to effect both QEC and Clifford-gate operations on the logical states of $|\mathcal{C}_L\rangle$. Initialization of $|\mathcal{C}_L\rangle$ to certain logical states and magic-state distillation are also possible by measurements that complete the universal set of gates for quantum computing.

Certain aspects of MTQC do bear some resemblance to the protocol in Ref. [28], which uses hybrid qubits as basic ingredients. However, this resemblance is only superficial. Since we use GHZ states as basic ingredients in MTQC, the very process of generating three-qubit resource states is different. The kind of entangling operations and apparatus employed are also very different. Here, we need on-off detectors, whereas the protocol in Ref. [28] requires photon-number-parity detectors. Additionally, MTQC exploits the concatenation of error-correcting codes to improve the tolerance against photon loss. In what follows, all stages of the MTQC scheme are discussed in detail.

A. Collective Bell-state measurement on multiphoton qubits

The Bell states of multiphoton qubits, each with n modes, are $|\phi_n^\pm\rangle = (|0_n 0_n\rangle \pm |1_n 1_n\rangle)/\sqrt{2}$, $|\psi_n^\pm\rangle = (|0_n 1_n\rangle \pm |1_n 0_n\rangle)/\sqrt{2}$. Interestingly, Bell states of multiphoton qubits can be decomposed as Bell states of individual photon modes, that is, $|\phi^\pm\rangle = (|HH\rangle \pm |VV\rangle)/\sqrt{2}$, $|\psi^\pm\rangle = (|HV\rangle \pm |VH\rangle)/\sqrt{2}$, as follows [41]:

$$|\phi_n^+\rangle = \frac{1}{\sqrt{2^{n-1}}} \sum_j \mathcal{P}_n[|\phi^+\rangle^{\otimes n-2j}, |\phi^-\rangle^{\otimes 2j}], \quad (3a)$$

$$|\phi_n^-\rangle = \frac{1}{\sqrt{2^{n-1}}} \sum_j \mathcal{P}_n[|\phi^+\rangle^{\otimes n-2j-1}, |\phi^-\rangle^{\otimes 2j+1}], \quad (3b)$$

$$|\psi_n^+\rangle = \frac{1}{\sqrt{2^{n-1}}} \sum_j \mathcal{P}_n[|\psi^+\rangle^{\otimes n-2j}, |\psi^-\rangle^{\otimes 2j}], \quad (3c)$$

$$|\psi_n^-\rangle = \frac{1}{\sqrt{2^{n-1}}} \sum_j \mathcal{P}_n[|\psi^+\rangle^{\otimes n-2j-1}, |\psi^-\rangle^{\otimes 2j+1}]. \quad (3d)$$

Here, for two states (or operators) A and B that are i - and $(n-i)$ -partite, respectively ($i \leq n$), and invariant under permutations of their supports, we define $\mathcal{P}_n[A, B] := \sum_{I \in S_{n,i}} A_I \otimes B_{\mathbb{Z}_n \setminus I}$, where $\mathbb{Z}_n := \{1, \dots, n\}$, $S_{n,i} := \{I \subseteq \mathbb{Z}_n : |I| = i\}$, and A_I indicates the state (or operator) A supported on I . As an example, if A and B are single-partite operators, $\mathcal{P}_4[A^{\otimes 2}, B^{\otimes 2}] = A \otimes A \otimes B \otimes B + A \otimes B \otimes A \otimes B + A \otimes B \otimes B \otimes A + B \otimes A \otimes A \otimes B + B \otimes A \otimes B \otimes A + B \otimes B \otimes A \otimes A$.

From the above expression, it is clear that if the states $|\phi^-\rangle$ and $|\psi^-\rangle$ can be distinguished at the mode level, all four Bell states can be identified at the logical level with success rate $1 - 2^{-n}$. Thus, as we add more photon modes to qubits, the success rate of BSMs on them improves and becomes near deterministic. The states $|\phi^-\rangle$ and $|\psi^-\rangle$ can be unambiguously distinguished by the BSM setup B_S shown in Fig. 1. If B_S registers an even (odd) number of $|\phi^-\rangle$ states, the corresponding state at the logical level is $|\phi_n^+\rangle$ ($|\phi_n^-\rangle$). On the other hand, if an even (odd) number of $|\psi^-\rangle$ states are registered, the corresponding state at the logical level is $|\psi_n^+\rangle$ ($|\psi_n^-\rangle$).

This scheme is robust against failure of bare BSM due to photon loss. Employing this scheme of near-deterministic collective BSM has another advantage over protocols that use multiple attempts of BSMs to entangle two optical smaller cluster states. In the latter case, the bare BSMs must be applied in a sequence and thus there is an associated waiting time for each of them during which photons may be lost. Also, when one of the BSMs succeed, the leftover photons must be trimmed from the star cluster state. Thus, the process also demands extensive usage of delay lines and switching networks. But in our case all the BSMs are applied simultaneously, removing the necessity for delay lines and switching networks, and the associated noise.

B. Resource states

Our protocol for MTQC begins with the creation of the following two kinds of multiphoton resource states:

$$|\mathcal{C}_3\rangle_{n,n,n} = \frac{1}{2}(|0_n 0_n 0_n\rangle + |0_n 0_n 1_n\rangle + |1_n 1_n 0_n\rangle - |1_n 1_n 1_n\rangle), \quad (4a)$$

$$|\mathcal{C}_{3'}\rangle_{n,m,n} = \frac{1}{\sqrt{2}}(|0_n 0_m 0_n\rangle + |1_n 1_m 1_n\rangle). \quad (4b)$$

These states are three-qubit entangled states at the logical level. Throughout the article, we suppose that $|\mathcal{C}_3\rangle_{n,n,n}$ has n polarization photons in all qubits, whereas $|\mathcal{C}_{3'}\rangle_{n,m,n}$ has n , m , and n polarization photons in the first, second, and

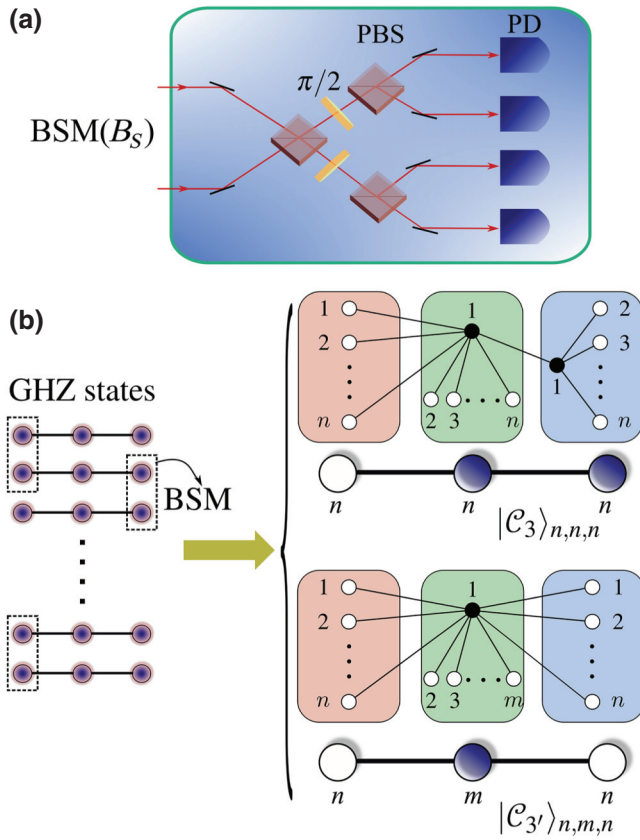


FIG. 1. (a) Bell-state measurement setup B_S consists of three polarization beam splitters (PBSs), two $\pi/2$ rotators, and four on-off photon detectors (PDs). We deem B_S to be successful when one of the first two PDs and one of the last two PDs click simultaneously. When successful, the setup can discriminate only two Bell states from four of them. Therefore, the success rate of B_S is $1/2$. (b) Resource states $|\mathcal{C}_3\rangle_{n,n,n}$ and $|\mathcal{C}_{3'}\rangle_{n,m,n}$ [see Eqs. (4)] can be generated using GHZ states from deterministic sources. We depict $|\text{GHZ}_3\rangle$, but $|\text{GHZ}_r\rangle$, where $r > 3$, can be used in principle. While all qubits of $|\mathcal{C}_3\rangle_{n,n,n}$ have n photons, the first, second, and third qubits of $|\mathcal{C}_{3'}\rangle_{n,m,n}$ have n , m , and n photons, respectively. The open circles refer to the qubits on which the Hadamard operation is carried out, as explained below Eqs. (4), and a solid line represents the existence of entanglement between the qubits. More refined pictures concerning the respective formations of $|\mathcal{C}_3\rangle_{n,n,n}$ and $|\mathcal{C}_{3'}\rangle_{n,m,n}$ states (both unitarily equivalent to graph states) are supplied here, where we intuitively note that $|\mathcal{C}_3\rangle_{n,n,n}$ is a result of a controlled- Z operation of two kinds of multiphoton GHZ states and $|\mathcal{C}_{3'}\rangle_{n,m,n}$ is itself a large multiphoton GHZ state. While a general formula for the number of GHZ states consumed to generate $|\mathcal{C}_3\rangle_{n,n,n}$ and $|\mathcal{C}_{3'}\rangle_{n,m,n}$ is absent, this may be explicitly calculated from the iterative procedure graphically presented in Fig. 2 and in Appendix B. See also Sec. VI for examples.

third qubits, respectively. One can verify that $|\mathcal{C}_3\rangle$ is the result of a Hadamard operation on the first qubit of the three-qubit linear cluster state $\text{CZ}_{1,2}\text{CZ}_{2,3}|+_n+_n+_n\rangle$. On the other hand, $|\mathcal{C}_{3'}\rangle$ is obtained by a Hadamard operation

on the first and third qubits of the same three-qubit linear cluster state and is a logical GHZ state.

The resource states are created by entangling r -photon GHZ states from deterministic sources using B_S , as shown in Fig. 1. This way of creating resource states using the B_S is possible when $r \geq 3$. Because of the usage of the B_S , the process is probabilistic and the required states are generated only when all the B_S succeed. If one of the B_S fails, the state is discarded and the process is restarted; that is, the repeat-until-success strategy is employed. This is also reflected in the resource overhead calculations carried out in Sec. VI. A successful B_S can distinguish $|\phi^+\rangle$ and $|\phi^-\rangle$. If the outcome is $|\phi^-\rangle$, a feed-forward Z operation would be necessary on a photon in resultant GHZ state. However, there is no need for physical implementation of this Z operation as such a feed-forward procedure can be realized by updating the *Pauli frame* [13]. Accordingly, measurement results on the photons must be interpreted in corroboration with the Pauli frame. On the other hand, failed BSMs make the involved GHZ states mixed, and thus they cannot be restored by feed-forward operations without additional resources. One solution is to use a suitable error-correction scheme to handle the failures, the discussion of which is beyond the scope of this article.

In this work, we consider $r = 3$, the smallest possible value, considering its experimental availability using current technology [37]. In principle, the $|\text{GHZ}_r\rangle$ states with $r > 3$ can be used at this stage, which would not only reduce the required number of B_S , but also improve resource efficiency (average number of incurred $|\text{GHZ}_r\rangle$ states) for generating $|\mathcal{C}_3\rangle_{n,n,n}$ and $|\mathcal{C}_{3'}\rangle_{n,m,n}$. However, a larger r would imply a poorer average fidelity of the GHZ states generated experimentally [37]. The state $|\mathcal{C}_3\rangle_{n,n,n}$ is created by entangling two $|\text{GHZ}_{n+1}\rangle$ states and a $H_{n+2}|\text{GHZ}_{n+2}\rangle$ state, where H_j is the Hadamard operator acting on the j th photon, using the B_S as shown in the final step of Fig. 2(a). The Hadamard operation is achieved by passing the polarization photons through a $\pi/2$ rotator. Similarly, the procedure to generate $|\mathcal{C}_{3'}\rangle_{n,m,n}$ is shown in Fig. 2(b). In this case no Hadamard operation is involved.

The states $|\text{GHZ}_{n+1}\rangle$ can be efficiently created by acting the B_S on the $|\text{GHZ}_3\rangle$ states in $\lceil \log_2(n-1) \rceil$ steps, as illustrated in Fig. 2. Here, $\lceil \cdot \rceil$ represents the ceiling of a number. For example, when the step number $k = 3$, up to $|\text{GHZ}_{10}\rangle$ (where $n+1 = 10$) can be created (other possible states are listed in Table II in Appendix B). The resource states $|\mathcal{C}_3\rangle_{n,m,n}$ and $|\mathcal{C}_{3'}\rangle_{n,m,n}$ are created with success rates $(2^{\lceil \log_2 n \rceil + 2})^{-1}$ and $(2^{\lceil \log_2(n-1) \rceil + 2})^{-1}$, respectively. At this stage of the protocol, delay lines and optical switches are employed. Delay lines are essential to delay the passage of photons that are not undergoing measurement until the action of the current B_S is complete. Therefore, quicker B_S 's permit shorter delay lines. Optical switches are needed to control the flow of photons through these delay lines, to choose the successful outputs

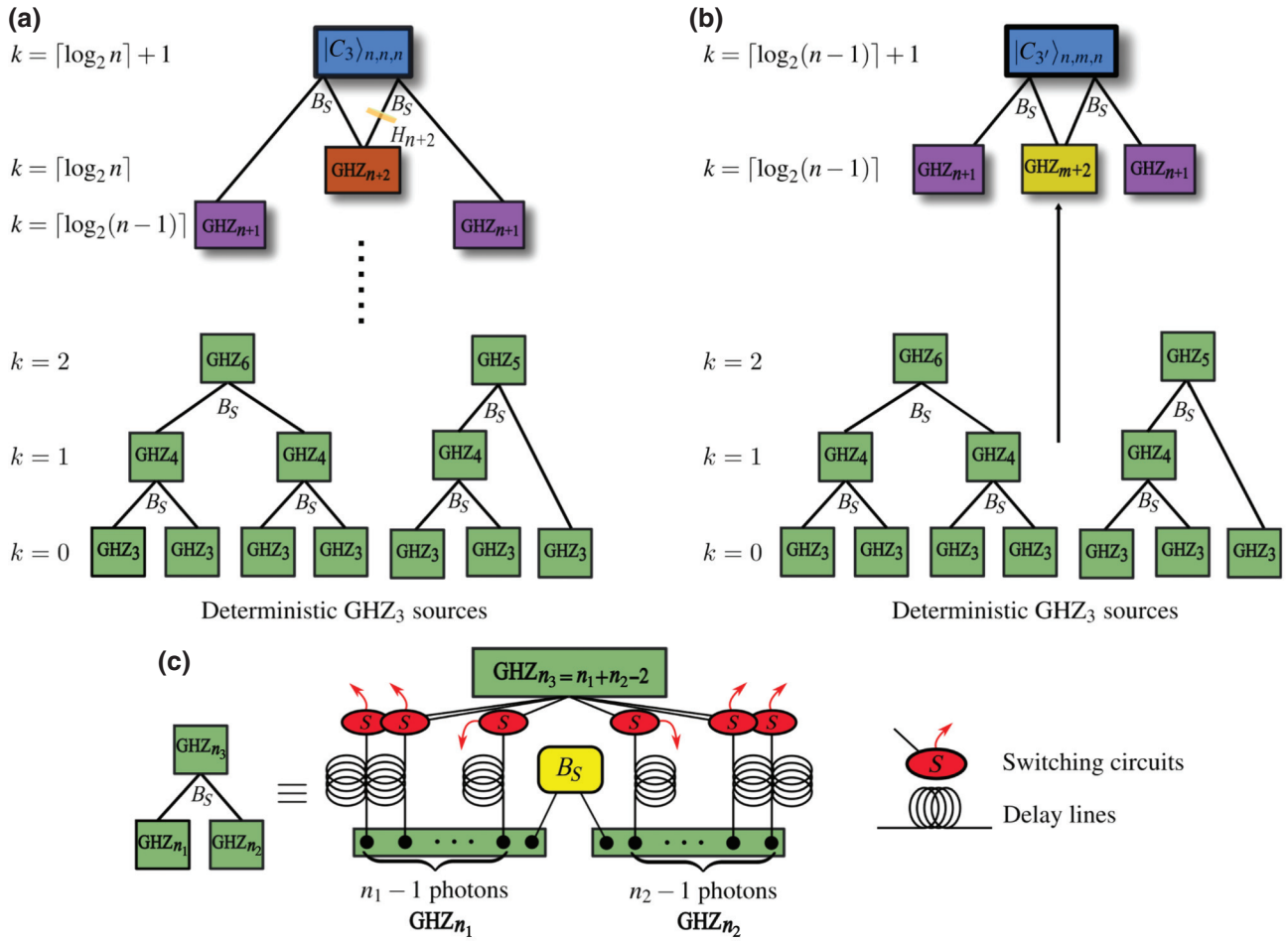


FIG. 2. Generation of resource states for MTQC. (a) The resource state $|\mathcal{C}_3\rangle_{n,n,n}$ [see Eq. (4a)] can be probabilistically generated by performing BSMs on $|\text{GHZ}_3\rangle$ states from deterministic sources in $\lceil \log_2 n \rceil + 1$ steps. It takes $k = \lceil \log_2 n \rceil$ steps to generate $|\text{GHZ}_{n+2}\rangle$ states. In the $(k + 1)$ th step two $|\text{GHZ}_{n+1}\rangle$ states are added from the step corresponding to a suitable value of k . In this step, Hadamard unitary operations on the last photon of $|\text{GHZ}_{n+2}\rangle$ (H_{n+2}) is performed before feeding it to B_S . This step involves two B_S 's and the $|\mathcal{C}_3\rangle_{n,n,n}$ state is formed only when both are successful. (b) To create $|\mathcal{C}'_3\rangle_{n,m,n}$, two $|\text{GHZ}_{n+1}\rangle$ states and a $|\text{GHZ}_{m+2}\rangle$ state (from a step of suitable k) are entangled, as shown without any Hadamard operation. Upon both B_S 's being successful, $|\mathcal{C}'_3\rangle_{n,m,n}$ is created. At the k th step, the largest possible GHZ state has $2^k + 2$ photons and other smaller GHZ states can be generated by entangling GHZ states from whichever previous steps, as depicted at $k = 2$. Smaller possible states are listed in Table II in Appendix B. Although the flowchart starts with $|\text{GHZ}_3\rangle$ as the basic ingredient, $|\text{GHZ}_r\rangle$ of any $r > 3$ may also be used in principle. In doing so, the value of k required to generate resource states can be reduced. In the case of encoding the qubits of $|\mathcal{C}_L\rangle$ with three-qubit repetition QEC codes, the $|\text{GHZ}_{m+2}\rangle$ states in the k th step are replaced by the $|\text{enc}\rangle$ [see Eq. (24)] to form the $|\mathcal{C}'_3\rangle_{\text{enc}}$ in Eq. (9). We refer the reader to Fig. 9 in Appendix C for the process of creating $|\text{enc}\rangle$. In the $(k + 1)$ th step $|\text{GHZ}_{n+2}\rangle$ is added from the step(s) corresponding to the lower value(s) of k . (c) Each action of B_S involves delay lines and switching networks. As an example, consider $|\text{GHZ}_{n_1}\rangle$ and $|\text{GHZ}_{n_2}\rangle$ being entangled to form $|\text{GHZ}_{n_3 = n_1 + n_2 - 2}\rangle$. The delay lines are employed to slow the passage of $n_3 = n_1 + n_2 - 2$ photons until the action of the B_S is complete. The switching network routes the leftover n_3 photons to the next level if B_S is successful. Otherwise, the photons are discarded.

of the B_S , and to send the larger GHZ states to the next step. Hence, many generation steps would entail a large number of optical switches and longer delay lines. Therefore, our resource-state generation protocol aims to minimize the usage of delay lines and optical switches that significantly contribute to photon loss. On the other hand, when deterministic sources capable of producing high-fidelity $|\text{GHZ}_r\rangle$ states with $r \geq 4$ are used, resource states can

be generated with a smaller number of time steps. The total number of steps to complete the generation of $|\mathcal{C}_3\rangle_{n,n,n}$ ($|\mathcal{C}'_3\rangle_{n,m,n}$) is $\lceil \log_2 n \rceil + 1$ [$\lceil \log_2(n-1) \rceil + 1$] when $m + 1 < n$.

Let us consider the creation of $|\mathcal{C}_3\rangle_{8,8,8}$ and $|\mathcal{C}'_3\rangle_{8,2,8}$ as an example. To create this state, we need to entangle $|\text{GHZ}_9\rangle$, $H_{10}|\text{GHZ}_{10}\rangle$, and $|\text{GHZ}_9\rangle$. All the required GHZ states are generated at the $(k = 3)$ th step using $|\text{GHZ}_3\rangle$ states. Upon

having successful B_S on the ninth photon of $|\text{GHZ}_9\rangle$ and first photon of $H_{10}|\text{GHZ}_{10}\rangle$, and on the tenth photon of $H_{10}|\text{GHZ}_{10}\rangle$ and first photon of $|\text{GHZ}_9\rangle$, we create $|\mathcal{C}_3\rangle_{8,8,8}$ in the ($k = 4$)th step. Similarly, when no H_{10} is performed and replacing $|\text{GHZ}_{10}\rangle$ with $|\text{GHZ}_4\rangle$, we end up having $|\mathcal{C}_3'\rangle_{8,2,8}$.

C. Star cluster states

After explaining the procedure to create resource states in detail, we now discuss the formation of the star cluster state $|\mathcal{C}_*\rangle$. Here, we use a near-deterministic n -Bell-state measurement (n -BSM) [41] that is a cascade of n B_S 's, as shown in Fig. 3(a), to entangle the resource states. An n -BSM fails when all the constituent B_S fail. Therefore, the success rate of n -BSM is $1 - 1/2^n$ and arbitrarily approaches 1 with increasing n . The working principle of an n -BSM is explained in Sec. II A. Two $|\mathcal{C}_3\rangle_{n,n,n}$ states and a $|\mathcal{C}_3'\rangle_{n,m,n}$ state are entangled using two n -BSMs to form a $|\mathcal{C}_*\rangle$, as shown in the Fig. 3(b). A $|\mathcal{C}_*\rangle$ is formed only when both the n -BSMs are successful in the process. In other failed cases, the desired $|\mathcal{C}_*\rangle$ is not formed and the resulting states are distorted, as shown in Figs. 3(c) and 3(d). A successfully generated $|\mathcal{C}_*\rangle$ will have m photons in the central qubit and n photons in the surrounding qubits. Having a larger n is desirable as the success rate of the n -BSM improves when the $|\mathcal{C}_*\rangle$ are entangled to form layers of $|\mathcal{C}_\mathcal{L}\rangle$. While having $m > 1$ suppresses the probability of qubit loss on $|\mathcal{C}_\mathcal{L}\rangle$ (as the qubit is redundantly encoded with multiple photons) during photon loss, it also invites stronger dephasing on the qubit, as described in Sec. III.

The n -BSM operations employed in our protocol scheme are surely prone to failures. At this point we introduce two subvariants of MTQC. In the first subvariant, referred to as MTQC-1, we do not employ any optical switches and use whatever star cluster states available upon failure of the n -BSMs. In the second subvariant, namely MTQC-2, we use the optical switch circuit to choose intact $|\mathcal{C}_*\rangle$ states and discard the distorted ones. This will make the photons pass through another delay line and switch. Thus, MTQC-1 adds one extra time step in creating $|\mathcal{C}_*\rangle$ while MTQC-2 adds two. To be explicit, until now the process of creating $|\mathcal{C}_\mathcal{L}\rangle$ has taken place in $k + 1$ and $k + 2$ time steps with MTQC-1 and MTQC-2, respectively. We study and compare the performances of both these subvariants in terms of photon-loss tolerance and resource efficiency.

D. Layers of the RHG lattice

The $|\mathcal{C}_*\rangle$ are entangled using n -BSMs to form layers of $|\mathcal{C}_\mathcal{L}\rangle$, as shown in Fig. 4. During the process, the surrounding qubits of each $|\mathcal{C}_*\rangle$ are consumed by the n -BSMs and the central qubit stays on the lattice. Upon a successful n -BSM, edges (representing entanglement) between the central qubits are formed. In MTQC-2 intact $|\mathcal{C}_*\rangle$ states

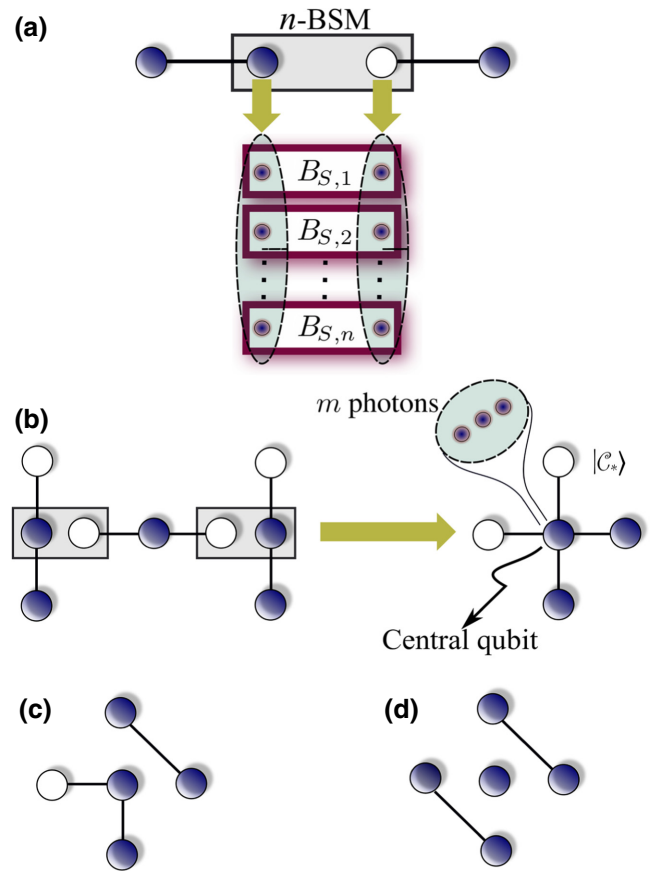


FIG. 3. (a) An n -BSM is used to create entanglement between two resource states. It consists of a cascade of n B_S 's acting on photons from two different n -photon qubits, as shown. The success rate of n -BSM increases with n as $1 - 2^{-n}$ (see Sec. II A), which makes it a near-deterministic entangling operation. (b) The star cluster state $|\mathcal{C}_*\rangle$ is generated by performing two n -BSMs on qubits of two $|\mathcal{C}_3\rangle_{n,n,n}$ states and a $|\mathcal{C}_3'\rangle_{n,m,n}$ state, as shown. The desired $|\mathcal{C}_*\rangle$ is formed only when both n -BSMs are successful. The resultant state (c) when one of the n -BSMs fails and (d) when both fail. The solid line represents the existence of entanglement between the qubits. The surrounding qubits are consumed by n -BSMs for creating entanglement between the central qubits (containing m photons) in the formation of $|\mathcal{C}_\mathcal{L}\rangle$. All central qubits contain lesser photons so that photon-loss-induced dephasing is reduced (see Sec. III).

are generated. If an n -BSM fails, the corresponding edge between the central qubits will be missing and such situations are handled by QEC on $|\mathcal{C}_\mathcal{L}\rangle$. For details on how missing edges on $|\mathcal{C}_\mathcal{L}\rangle$ are handled, we refer the reader to Refs. [15,48]. However, in MTQC-1, distorted $|\mathcal{C}_*\rangle$ states are allowed and this gives rise to $|\mathcal{C}_\mathcal{L}\rangle$ with *diagonal* edges [see also Fig. 2(c) of Ref. [28]] along with missing edges. The diagonal edges distort the local RHG structure, which in turn makes the usual error syndrome extraction impossible. This too, like the problem of missing edges, is overcome by QEC where qubits associated with diagonal edges are removed. Therefore, the state ket $|\mathcal{C}_\mathcal{L}\rangle$ generated

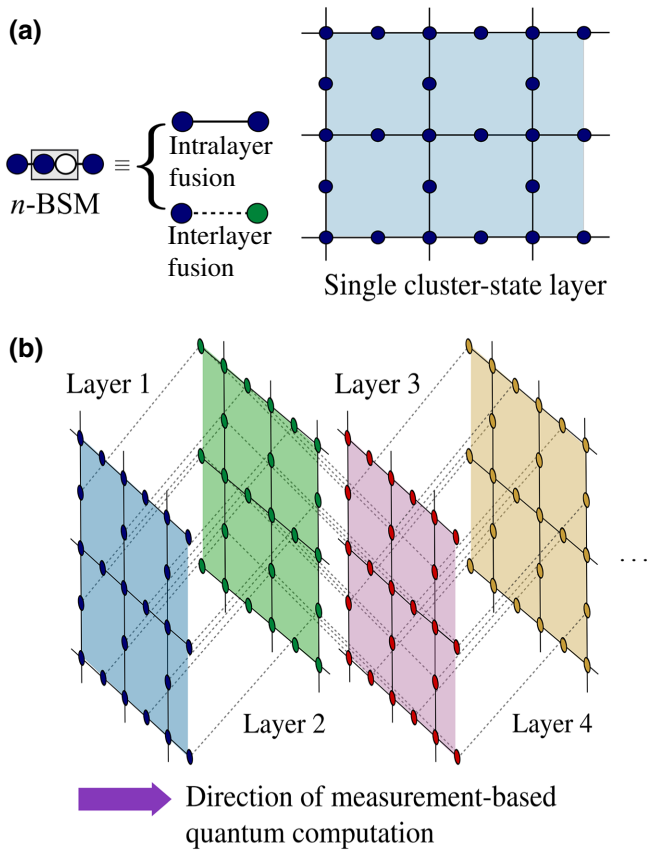


FIG. 4. (a) Each layer of the RHG lattice is generated by entangling the star cluster states $|\mathcal{C}_*\rangle$ using n -BSMs. (b) An implementation scheme where multiple layers that form $|\mathcal{C}_\mathcal{L}\rangle$ can be created in time through interlayer n -BSMs.

in MTQC-1 would have more missing qubits (explained in detail in Sec. V), and is thus of a poorer quality. We emphasize that at this stage in the formation of layers in MTQC, no optical switch is involved in either protocol subvariant.

In MTQC-1 the formation of $|\mathcal{C}_\mathcal{L}\rangle$ and $|\mathcal{C}_*\rangle$ takes place simultaneously; that is, both happen in the $(\lceil \log_2 n \rceil + 2)$ th time step. But in MTQC-2 the formation of $|\mathcal{C}_\mathcal{L}\rangle$ happens in the next time step after the intact $|\mathcal{C}_*\rangle$ are formed. Therefore, $|\mathcal{C}_\mathcal{L}\rangle$ is formed in the $(\lceil \log_2 n \rceil + 3)$ th time step. Another point to be noted is that the qubits of $|\mathcal{C}_*\rangle$ that take part in entangling to a future layer must wait for an extra time step. This completes the protocol for generating $|\mathcal{C}_\mathcal{L}\rangle$.

E. Universal quantum computing on the RHC lattice

Following the RHG-lattice generation, where a faulty $|\mathcal{C}_\mathcal{L}\rangle$ with missing edges and phase-flip errors is created, topological fault-tolerant quantum computing is carried out by making sequential single-qubit measurements in X and Z bases as dictated by the quantum gates being implemented. Measurements in the Z basis remove qubits from $|\mathcal{C}_\mathcal{L}\rangle$, creating *defects* that also create logical states

of the lattice. These defects are braided to achieve two-qubit logical operations topologically [33,34]. The X -basis measurement outcomes provide error syndromes and also effect Clifford gates on the logical states. The universal set of operations for quantum computing is complete with the inclusion of *magic-state distillation* for which measurements on the chosen qubits are carried out in the $(X \pm Y)/\sqrt{2}$ basis [33,34]. Practically, Z -basis measurements on qubits are possible by measuring the polarization of any photon belonging to the qubit in the z direction. On the other hand, an X -basis measurement outcome of a lattice qubit is given by the parity of X -basis measurements of the constituent photons.

Logical errors on $|\mathcal{C}_\mathcal{L}\rangle$ occur when a chain of Z operators connects two defects or encircles a defect. Code distance d (lattice size) is the minimum number of Z operations on the lattice qubits such that two defects are connected. In the following we explain how random Z operators (errors) on optical qubits happen due to photon loss. These errors coupled with wrong inference in decoding during QEC go undetected and will lead to logical errors [33,34]. We refer the reader to Appendix A for more details on logical errors. The logical errors are faulty gate operations and can be minimized by choosing sufficiently large d . If p_L denotes the logical error rate, our aim is to reduce it to a target error rate, p_L^{targ} , set by the end user.

III. NOISE MODEL

Apart from photon loss being a major source of errors [2], the lattice $|\mathcal{C}_\mathcal{L}\rangle$ built with linear optics suffers from missing edges due to probabilistic entangling operations. In this section, we study the effects of photon loss on the success rate of entangling operations, and consequently, the MTQC protocol. Suppose that the overall photon-loss rate suffered by each photon due to imperfect optical components is η and that the initial state of an l -photon qubit is defined by $|\Psi^l\rangle = \alpha|H\rangle^{\otimes l} + \beta|V\rangle^{\otimes l}$. When η is nonzero, the state of the multiphoton qubit is [41]

$$\begin{aligned} \tilde{\rho}_l = & |\Psi^l\rangle(1-\eta)^l\langle\Psi^l| + \frac{1}{2} \sum_{q=1}^l \eta^q(1-\eta)^{l-q} \\ & \times \mathcal{P}_l[|\Psi^{l-q}\rangle\langle\Psi^{l-q}| + |\Psi_{-}^{l-q}\rangle\langle\Psi_{-}^{l-q}|, |\text{VAC}_q\rangle\langle\text{VAC}_q|], \end{aligned} \quad (5)$$

where $|\Psi_{-}^{l-q}\rangle = \alpha|H\rangle^{\otimes l-q} - \beta|V\rangle^{\otimes l-q}$ and $|\text{VAC}_q\rangle$ is a vacuum state. The probability of an l -photon qubit losing one or more photons is $1 - (1-\eta)^l$. When photons are lost, with probability 0.5, the state possesses the component $|\Psi_{-}^l\rangle\langle\Psi_{-}^l|$, that is, undergoes dephasing.

If $0 \leq \eta \leq 1$ is the overall photon-loss rate due to an imperfect GHZ source (η^{soc}), delay lines (η^{dly}), an optical switching network (η^{swc}), and detectors (η^{det}), the rate of

dephasing on the multiphoton lattice qubits due to photon loss is

$$p_Z = \frac{1 - (1 - \eta)^l}{2}. \quad (6)$$

If photon losses in different components of quantum computing are statistically independent, we have the relation

$$\eta = 1 - (1 - \eta^{\text{soc}})(1 - \eta^{\text{dly}})(1 - \eta^{\text{swc}})(1 - \eta^{\text{det}}), \quad (7)$$

which associates the overall photon-loss rate to the relevant individual component loss rates. For the delay lines $(1 - \eta^{\text{dly}}) = e^{-c\tau_0\kappa/L_0}$, where $L_0 = 22$ km is the attenuation length of an optical fiber for the standard telecom wavelength of 1550 nm [59], $c = 2 \times 10^5$ km/s is the speed of light in, say acrylic (PMMA) optical fibers, $\tau_0 = 150 \times 10^{-9}$ s [2] is the time duration to complete one BSM, which can be made smaller using electro-optical modulators, and κ is the total number of time steps (in units of τ_0) a lattice-qubit or, equivalently, a central qubit of $|\mathcal{C}_*\rangle$ spends before being measured during fault tolerant quantum computing. Also, each photon has to pass through a network of κ switches. Therefore, $\eta^{\text{swc}} = 1 - (1 - \eta^{\text{s}})^\kappa$, where η^{s} is the photon-loss rate through one optical switch. It is important to note from Eq. (6) that photon loss introduces a larger rate of dephasing on qubits with a larger number of photons.

The B_S operates on the lossy states and, when input photons are lost, the failure rate increases to $1 - (1 - \eta)^2/2$. An n -BSM would fail only when all the constituent B_S fail. Therefore, the failure rate of an n -BSM due to photon loss is

$$p_f = \left[1 - \frac{(1 - \eta)^2}{2} \right]^n \underset{\eta \ll 1}{\cong} \left(\frac{1}{2} + \eta \right)^n. \quad (8)$$

From the above expression, we observe that, when η is $O(10^{-2})$ and n is large, p_f is not very sensitive to photon loss.

We point out that, like other DV optical schemes [17], photon loss does not necessarily imply lattice-qubit loss. The probability that photon loss leads to lattice-qubit loss, η^m , is much smaller than p_f for $\eta \sim 10^{-2}$, $n \geq 5$, and $m \geq 2$ considered in this work. Therefore, n -BSM failure has a dominant effect over qubit loss when calculating the *logical error rate* on $|\mathcal{C}\rangle_{\mathcal{L}}$ and the latter can be neglected. However, having large m is not favorable as it invites stronger dephasing, as inferred from Eq. (6). To mitigate this issue, we set $m = 2$ throughout the work, which is also sufficient to neglect the effect of qubit loss.

The MTQC is operated at the same photon-loss rate η on all qubits and the number of photons in lattice qubits is $m = 2$. In this case $\kappa < k$ and it is crucial to note that the lattice qubits always spend $\kappa = 3(4)$ time

steps in MTQC-1 (MTQC-2) before being measured. Now one can appreciate that our protocol to generate $|\mathcal{C}_{3'}\rangle_{n,2,n}$ makes sure that the photons of lattice qubits pass through the least number of optical components. Therefore, for a fixed η , componentwise photon-loss tolerance of MTQC is enhanced. Also, note that before performing n -BSMs to form $|\mathcal{C}_{\mathcal{L}}\rangle$, the *surrounding* qubits of a $|\mathcal{C}_*\rangle$ have to pass through a larger number of lossy components as $n > m$ and therefore have a larger photon-loss rate. Moreover, qubits that are part of the n -BSM between the current and future layers spend an extra time step and thus suffer from stronger losses. However, this time delay depends on the physical architecture that runs measurement-based quantum computation along with other technological details; in principle, different layers can be generated simultaneously. Therefore, we hereby neglect the influence of time delays on η , which is reasonable if the time delay is sufficiently shorter than $-(L_0/c) \ln \eta$.

For the star cluster states, qubit dephasing owing to photon loss happens *locally* on the central and other qubits. In addition, the surrounding qubits are consumed during an n -BSM and noise owing to photon loss can be dealt with by suitably encoding these qubits. Investigation of this procedure is the subject of our future work that is beyond the scope of this article. In this work, we consider only the dephasing noise due to photon loss on the central qubits. One can also consider other kinds of amplitude-damping noise [60–63] to evaluate the performance of our MTQC protocols.

IV. ENCODING LATTICE QUBITS WITH THE REPETITION CODE

As described in the previous section, photon loss leads to dephasing on the qubits. We observe from Eq. (6) that if the degree of dephasing can be reduced, MTQC can have a larger photon-loss threshold η_{th} . To reduce the effect of dephasing, one intuitive approach would be to encode the qubits of $|\mathcal{C}_{\mathcal{L}}\rangle$ with a multiqubit repetition code. This can be achieved by encoding the m -photon qubits of resource ket $|\mathcal{C}_{3'}\rangle_{n,m,n}$ with an N -qubit repetition code; one would replace $|0_m\rangle$ with $(|0_m\rangle + |1_m\rangle)^{\otimes N}$, and $|1_m\rangle$ with $(|0_m\rangle - |1_m\rangle)^{\otimes N}$ (up to normalization), where N is the repetition number. This gives the following encoded resource ket:

$$|\mathcal{C}_{3'}\rangle_{\text{enc}} = |0_n\rangle(|0_m\rangle + |1_m\rangle)^{\otimes N}|0_n\rangle + |1_n\rangle(|0_m\rangle - |1_m\rangle)^{\otimes N}|1_n\rangle. \quad (9)$$

Note that the extreme qubits, each holding n photons, are not encoded as they will be consumed by n -BSMs anyway.

As an example for demonstrating that we can increase η_{th} , let us consider $N = 3$. The generation of the encoded $|\mathcal{C}_{3'}\rangle$ kets using $|\text{GHZ}_3\rangle$ states and B_S is explained in Appendix C. The QEC procedure using this three-qubit repetition code employs the *majority voting* strategy,

which fails when two or more qubits undergo dephasing [9]. Thus, the effective dephasing rate due to photon loss on the encoded lattice qubits is

$$p_{Z,\text{enc}} = 3p_Z^2(1 - p_Z) + p_Z^3, \quad (10)$$

where p_Z is the unencoded dephasing error from Eq. (6). It is clear that $p_{Z,\text{enc}} < p_Z$ when $p_Z < 0.5$. Hence, such a repetition encoding can suppress the dephasing rate, which would result in an improvement of η_{th} . The new tolerable photon-loss rate, $\eta_{\text{th}}^{\text{enc}}$, is deduced by inverting the expression for $p_{Z,\text{enc}}$. In principle, we can make $\eta_{\text{th}}^{\text{enc}}$ arbitrarily close to 1 by increasing the value of N . This encoding strategy would evidently require more GHZ ingredient states to generate *encoded* (star) cluster states. However, as we will see in Sec. VI, numerical simulations show that using encoded states also reduces the effective dephasing rate (implying a larger tolerable photon-loss rate) to an extent that outweighs the additional GHZ states needed for encoding, such that smaller values of d would suffice to reach p_L^{targ} .

We now suppose that the lattice qubit is encoded with a *finite* N -qubit repetition code [9]. Using majority voting, the effective dephasing rate on the encoded lattice qubits is

$$p_{Z,\text{enc}} = \sum_{q=\lceil(N+1)/2\rceil}^N \binom{N}{q} p_Z^q (1 - p_Z)^{N-q}, \quad (11)$$

where p_Z is the dephasing rate on unencoded lattice qubits. The task is to reveal the influence of N on the value of the photon-loss threshold rate η_{th} .

We make use of the convenient approximation

$$\begin{aligned} & \binom{N}{q} p_Z^q (1 - p_Z)^{N-q} \\ & \cong \frac{\exp\{-(q - Np_Z)^2/[2Np_Z(1 - p_Z)]\}}{\sqrt{2\pi Np_Z(1 - p_Z)}}, \end{aligned} \quad (12)$$

which is valid for sufficiently large N owing to the central limit theorem. After a variable substitution with $x = q/N$, this allows us to convert Eq. (11) into an integral,

$$\begin{aligned} p_{Z,\text{enc}} & \cong \int_{1/2}^{\infty} dx \frac{\exp\{-(x - p_Z)^2/[2p_Z(1 - p_Z)/N]\}}{\sqrt{2\pi p_Z(1 - p_Z)/N}} \\ & = \frac{1}{2} - \frac{1}{2} \operatorname{erf}\left(\frac{1 - 2p_Z}{2\sqrt{2p_Z(1 - p_Z)/N}}\right), \end{aligned} \quad (13)$$

which involves the error function $\operatorname{erf}(\cdot)$. The infinite upper limit of the integral is justified by the extremely narrow width of the Gaussian integrand for large N . Since, for a

large argument z ,

$$\operatorname{erf}(z) \cong 1 - \frac{e^{-z^2}}{\sqrt{\pi}z}, \quad (14)$$

we get $ye^{y^2/8} \cong \sqrt{2/\pi}/p_{Z,\text{enc}}$, where $y = (1 - 2p_Z)/\sqrt{p_Z(1 - p_Z)/N}$. Squaring this relation allows us to write

$$y^2 \cong 4W(1/(2\pi p_{Z,\text{enc}}^2)), \quad (15)$$

which expresses the solution as a Lambert function $W(\cdot)$. This leads to the physical solution

$$p_Z \cong \frac{1}{2} - \frac{1}{2\sqrt{1+4t}}, \quad t = \frac{N}{4W(1/(2\pi p_{Z,\text{enc}}^2))}. \quad (16)$$

We may now immediately identify $(1 - \eta_{\text{th}}^{\text{enc}})^m \cong (1 + 4t)^{-1/2}$, with m being the number of photons of each qubit in the repetition code, which finally yields

$$\eta_{\text{th}}^{\text{enc}} \cong 1 - \left[1 + \frac{N}{W(1/(2\pi p_{Z,\text{enc}}^2))}\right]^{-1/(2m)}. \quad (17)$$

As N increases, we find that $\eta_{\text{th}}^{\text{enc}} \cong 1 - O(1/N^{1/(2m)}) \rightarrow 1$ for any designated values of $p_{Z,\text{enc}} < p_Z$ and m . On the other hand, the function $W(1/(2\pi p_{Z,\text{enc}}^2))$ itself is a slowly increasing function of $p_{Z,\text{enc}}$ as $p_{Z,\text{enc}}$ decreases, originating from the large-argument expansion

$$W(x) \cong \ln x - \ln \ln x + \frac{\ln \ln x}{\ln x} + \frac{(\ln \ln x - 2) \ln \ln x}{2(\ln x)^2}, \quad (18)$$

so that within the typical range $0.001 \leq p_{Z,\text{enc}} \leq 0.1$ of interest, the order of magnitude for $W(1/(2\pi p_{Z,\text{enc}}^2))$ does not change. For a repetition code of fixed N and a given $p_{Z,\text{enc}}$, increasing m reduces $\eta_{\text{th}}^{\text{enc}}$.

V. RESULTS ON THE PHOTON-LOSS THRESHOLD

When carrying out QEC on $|\mathcal{C}_L\rangle$, the logical error rate p_L is determined against p_Z for various code distances d via simulation. This procedure is repeated for various values of n , which determine the respective p_f of the n -BSMs. The intersection point of the curves corresponding to various d is the threshold dephasing rate $p_{Z,\text{th}}$ as marked in Fig. 5. The photon-loss threshold η_{th} is determined using Eq. (6) by replacing p_Z with $p_{Z,\text{th}}$.

For example, from Fig. 5, which corresponds to $n = 8$, we have $p_{Z,\text{th}} \approx 2.9 \times 10^{-2}$ (3.2×10^{-2}) for MTQC-1 (MTQC-2). Considering that MTQC is operated below the threshold value (see Table I) at $\eta = 0.01$, according to Eq. (8), we then have the associated value

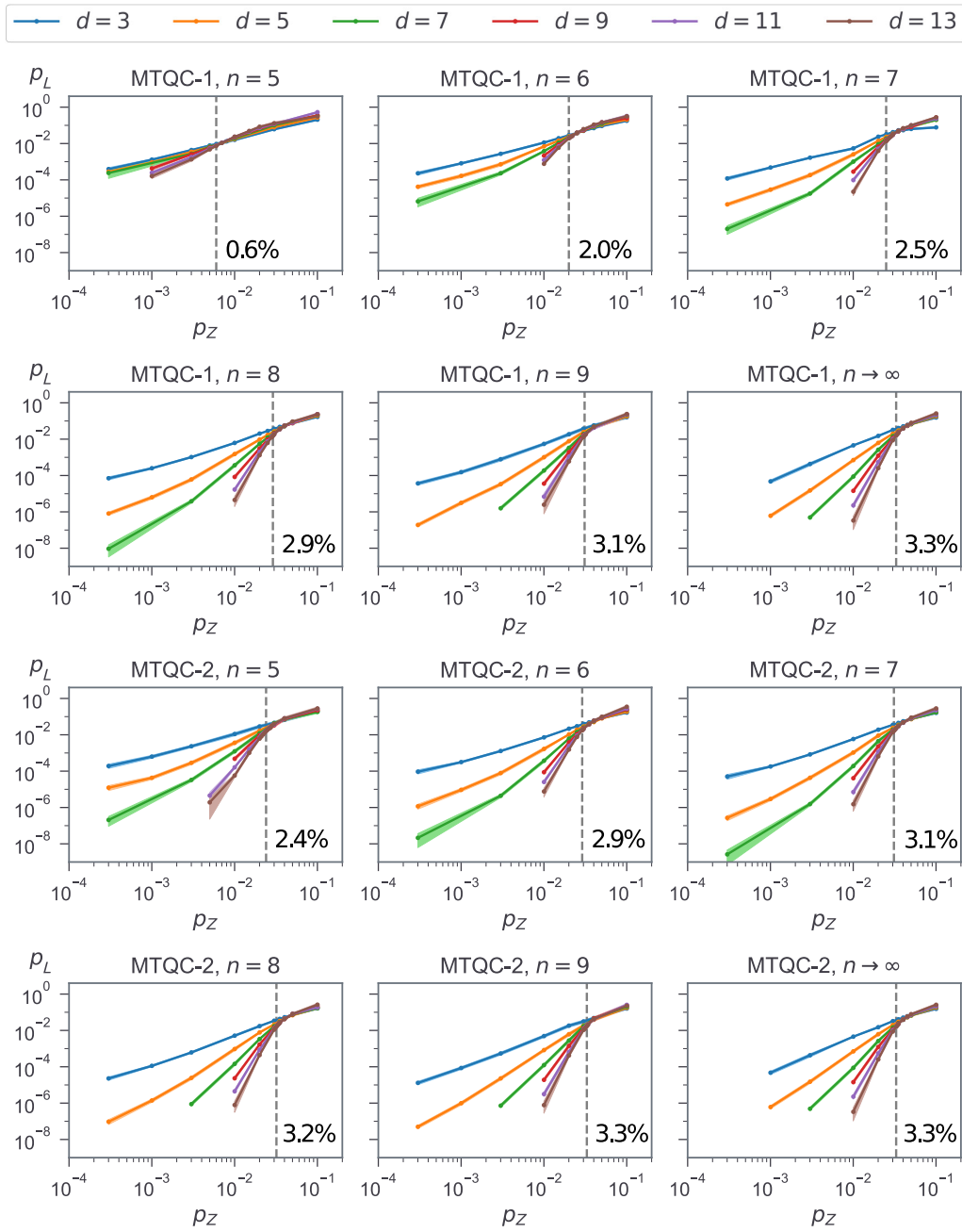


FIG. 5. Logical error rate p_L plotted against the dephasing rate p_z for MTQC-1 and MTQC-2 with $n \in [4, 9]$, where $m = 2$, accompanied by 99% confidence intervals (shaded regions) that are typically much narrower than the average values. For each n value, we plot p_L corresponding to code distances (RHG lattice size) $d = 3, 5, 7, 9, 11, 13$. The intersection point of the p_L curves for various d values corresponds to the threshold dephasing rate $p_{z,\text{th}}$. We observe that, as n increases, the failure rate of the n -BSMs, p_f , decreases, leading to a larger $p_{z,\text{th}}$. It is important to note that, when $n = 9$, $p_{z,\text{th}}$ is close to that in the $p_f = 0$ case, so that considering $n > 9$ results in no visible advantage. The threshold value η_{th} is shown for every figure panel.

of $p_f = 4.58 \times 10^{-3}$. Replacing p_z by $p_{z,\text{th}}$ in Eq. (6) we find that the total tolerable photon-loss rate η_{th} is 2.9×10^{-2} (3.2×10^{-2}) for MTQC-1 (MTQC-2). However, the photon-loss rate tolerable by individual components can be deduced as follows. The total time steps spent by lattice qubits before being measured is $\kappa = 3$ (4)

for MTQC-1 (MTQC-2). Therefore, we have $\eta_{\text{dly}} = 4.1 \times 10^{-3}$ (5.4×10^{-3}). Furthermore, by inserting the value of η_{dly} in Eq. (7) ($m = 2$), we have $\eta_{\text{th}}^{\text{soc}} = \eta_{\text{th}}^{\text{swc}} = \eta_{\text{th}}^{\text{det}} = 8.6 \times 10^{-3}$ (8.8×10^{-3}) for MTQC-1 (MTQC-2). This implies that equal amounts of photon loss can be tolerated in the GHZ source, optical switches, and measurement.

In this case each switch in the network can tolerate a photon-loss rate of $\eta^s = 2.8 \times 10^{-3}$ (1.7×10^{-3}). While the η_{th} in MTQC-2 is higher, both subvariants offer comparable componentwise photon-loss thresholds. However, MTQC-2 imposes more stringent restriction on the allowed photon-loss rate in switches. We lastly note that the time delays between consecutive layers can be neglected if they are sufficiently shorter than $-(L_0/c) \ln \eta_{\text{th}} \approx 4 \times 10^{-4}$ s for both MTQC-1 and MTQC-2, as discussed in Sec. III.

The η^{soc} , η^{swc} , and η^{det} are complementary in nature as the overall tolerable photon-loss rate of the MTQC is fixed. Therefore, if the GHZ source and detectors are operated at lower loss levels, the MTQC protocol can tolerate a much higher photon-loss rate in the optical switches. Similarly, we have repeated the calculation for $n = 5$ through 9, and the values of η_{th} are tabulated in Table I. We know from Ref. [48] that, when $p_f = 0.145$ in MTQC-2, the $|\mathcal{C}_{\mathcal{L}}\rangle$ cannot tolerate any dephasing, and hence any photon loss. This threshold p_f is overcome when $n \geq 3$. However, the situation is different for MTQC-1 and is explained in the following.

In MTQC-1, distorted $|\mathcal{C}_*\rangle$ states are allowed and this gives rise to $|\mathcal{C}_{\mathcal{L}}\rangle$ with *diagonal* edges [see also Fig. 2(c) of Ref. [28]]. This is overcome by removing the qubits at the ends of a diagonal edge during QEC. Therefore, the probability that a qubit survives on $|\mathcal{C}_{\mathcal{L}}\rangle$ is $1 - p_f$. Note also that each qubit in $|\mathcal{C}_{\mathcal{L}}\rangle$ is susceptible to losses from diagonal edges connected to *four* $|\mathcal{C}_*\rangle$ states: two in the layer containing the qubit, and another two coming from different layers. Additionally, failure of an n -BSM that connects two $|\mathcal{C}_*\rangle$ states would leave an edge between qubits missing. This situation is handled by removing one of the qubits associated with such a missing edge [48]. The survival probability of a lattice qubit in this case is $1 - p_f/2$, where *four* n -BSMs are involved. It follows that the total probability of losing a qubit on $|\mathcal{C}_{\mathcal{L}}\rangle$ is $1 - (1 - p_f)^4 (1 - p_f/2)^4$ and this number should not exceed 0.249 [55,64] if $|\mathcal{C}_{\mathcal{L}}\rangle$ should be useful for quantum computing. Therefore, the threshold value for p_f is 0.047, which is determined by solving the equation $1 - (1 - p_f)^4 (1 - p_f/2)^4 = 0.249$. So, MTQC-1 is possible only when $n \geq 5$. Note that lattices other than the RHG type have different values for threshold failure rates of the entangling operation [65,66]. Accordingly, the probability of missing qubits in MTQC-2 is $1 - (1 - p_f)^4$. For a given value of p_f , the resulting lattice in MTQC-1 has more missing qubits and is therefore of a relatively poorer quality.

The tolerable photon-loss thresholds for MTQC naturally increase with the usage of repetition codes in the manner discussed in Sec. IV. Let us consider an example of an encoded lattice qubit with $n = 8$, $m = 2$, and $N = 3$. In this encoded situation, The value for the overall photon-loss threshold using a three-qubit repetition code, obtained by using Eq. (10), is $\eta_{\text{th}}^{\text{enc}} = 10.7\%$ (11.1%) for MTQC-1 (MTQC-2). In this example $\kappa = 6$ (7), following which

we have $\eta_{\text{dly}} = 8.1 \times 10^{-3}$ (9.5×10^{-3}). The componentwise tolerance would be 3.2×10^{-2} (3.4×10^{-2}). In other words, encoding the lattice qubits with a three-qubit repetition code increases the η_{th} by nearly 4 times. Also, each switch can now tolerate a higher $\eta^s = 5.4 \times 10^{-3}$ (4.9×10^{-3}). The results for other values of n are available in Table I. Additionally, a sufficiently large set of stabilizer measurements on encoded qubits can be used to reconstruct the underlying noisy quantum process acting on these qubits [67,68].

VI. RESULTS ON THE RESOURCE OVERHEAD

In this work, we consider GHZ states as the raw ingredients for constructing $|\mathcal{C}\rangle_{\mathcal{L}}$, on which fault-tolerant gate operations are performed via single-qubit measurements. Therefore, the resource overhead \mathcal{N} is the average number of $|\text{GHZ}\rangle$ states consumed to build $|\mathcal{C}\rangle_{\mathcal{L}}$ to the required size. Other components used in MTQC, such as delay lines, detectors, optical switches, and beam splitters, scale proportionately to \mathcal{N} . Alternatively, Li *et al.* [18] considered detectors to be resources. Logical gate operations are possible by passing defects through $|\mathcal{C}\rangle_{\mathcal{L}}$ [33,34]. As logical errors occur when a chain of Z errors connects two defects or encircles a defect, error-free operations would demand that these defects be separated by a distance d and that they also have a perimeter of d . When noise is below threshold, by increasing the value of d , the logical error rate p_L can be reduced arbitrarily. If $|\mathcal{C}\rangle_{\mathcal{L}}$ has sides of length $l = 5d/4$, it can accommodate a defect of perimeter d and other defects placed a distance d apart from each other (see Fig. 8 of Ref. [29]).

The time for simulation of QEC on $|\mathcal{C}\rangle_{\mathcal{L}}$ increases drastically with d , rendering the estimation of (a very small) p_L for arbitrarily large d unfeasible. So, the value of d at which an extremely small target p_L (p_L^{targ}) is achieved can be estimated by extrapolating known values of p_L . We can determine the target d required to achieve $p_L^{\text{targ}} = 10^{-6}$ and 10^{-15} using the expression [56]

$$p_L^{\text{targ}} = b \left(\frac{a}{b} \right)^{-(d-d_b)/2}, \quad (19)$$

where a and b are the values of p_L corresponding to the second largest d_a and the largest code distance d_b , respectively, considered in our simulations. For example, as seen from Fig. 5, when $p_Z = 0.01$, we have $d_a = 11$ and $d_b = 13$.

As a practice, for $n > 5$, we operate MTQC at $\eta = 0.01$, which is below the photon-loss threshold value. This corresponds to $p_Z \approx 0.01$ at $m = 2$ for the unencoded case and $p_{Z,\text{enc}} \approx 3 \times 10^{-4}$ for the encoded one. However, unencoded MTQC-1 with $n = 5$ yields a threshold rate of $\eta_{\text{th}} \approx 6 \times 10^{-3}$ and is thus operated at $\eta = 3 \times 10^{-3}$. Therefore, the $\mathcal{N}_{p_L^{\text{targ}}}$ is also determined at the operation point. In

TABLE I. Table of values for the dephasing-noise threshold $p_{Z,\text{th}}$, photon-loss threshold η_{th} , and resource overhead $\mathcal{N}_{p_L}^{(\prime)\text{targ}}$ to achieve $p_L^{\text{targ}} = 10^{-6}$ and 10^{-15} concerning various instances n of our scalable MTQC-1 and MTQC-2 protocols. The improvement in the photon-loss threshold by encoding all lattice qubits with the ($N = 3$)-qubit repetition QEC code, $\eta_{\text{th}}^{\text{enc}}$, and their associated resource overhead, $\mathcal{N}_{p_L}^{(\prime)\text{enc}}$, are also listed for comparison. The table starts from $n = 5$ since MTQC-1 is not possible when $n \leq 4$, as detailed in Sec. V. The benefits of encoding is apparent both in terms of η_{th} and resource overheads. The asymptotically achievable value of p_{th} when $p_f = 0$ is 0.033 (see Fig. 5). Therefore, increasing n beyond 9 gives no visible advantage. However, $\eta_{\text{th}}^{\text{enc}}$ can be arbitrarily improved by increasing the repetition number N in the encoding of lattice qubits. As expected, increasing the value of n generally improves η_{th} and $\eta_{\text{th}}^{\text{enc}}$. Interestingly, $\mathcal{N}_{p_L}^{\text{targ}}$ reduces with n until $n = 8$, beyond which the excessive amount of $|\text{GHZ}_3\rangle$ states required for resource-state generation quickly nullifies any subsequently insignificant improvement in η_{th} . In view of this, we conclude that MTQC-2 with $n = 8$ is the optimal case of unencoded MTQC. Note that the resource overheads are calculated when MTQC operates at $\eta = 0.01$, which corresponds to $p_Z = 0.01$ and $p_{Z,\text{enc}} = 0.0003$. A similar practice is adopted in Ref. [34], where “operational overheads” are computed “at 1/3 of the fault-tolerance threshold.”

n	MTQC-1							MTQC-2						
	$p_{Z,\text{th}}$	η_{th} (%)	$\eta_{\text{th}}^{\text{enc}}$ (%)	$d_{10^{-6}}$ $d_{10^{-15}}$	$\mathcal{N}_{10^{-6}}$ $\mathcal{N}_{10^{-15}}$	$d_{10^{-6}}^{\text{enc}}$ $d_{10^{-15}}^{\text{enc}}$	$\mathcal{N}_{10^{-6}}^{\text{enc}}$ $\mathcal{N}_{10^{-15}}^{\text{enc}}$	$p_{Z,\text{th}}$	η_{th} (%)	$\eta_{\text{th}}^{\text{enc}}$ (%)	$d_{10^{-6}}$ $d_{10^{-15}}$	$\mathcal{N}'_{10^{-6}}$ $\mathcal{N}'_{10^{-15}}$	$d_{10^{-6}}^{\text{enc}}$ $d_{10^{-15}}^{\text{enc}}$	$\mathcal{N}'_{10^{-6}}^{\text{enc}}$ $\mathcal{N}'_{10^{-15}}^{\text{enc}}$
5	0.006	0.6	4.6	53 168	1.13×10^9 3.66×10^{10}	39 162	7.40×10^8 5.5×10^{10}	0.024	2.4	9.7	21 61	7.66×10^7 1.91×10^9	7 22	3.42×10^6 1.47×10^8
6	0.02	2.0	8.7	41 128	8.91×10^8 2.74×10^{10}	9 34	1.47×10^7 6.82×10^8	0.029	2.9	10.7	17 51	5.90×10^7 1.76×10^9	5 15	2.42×10^6 5.66×10^7
7	0.025	2.5	9.9	19 58	1.34×10^8 3.56×10^9	6 19	4.73×10^6 1.45×10^8	0.031	3.0	10.9	15 42	5.58×10^7 1.29×10^9	5 13	2.13×10^7 4.46×10^7
8	0.029	2.9	10.7	15 47	8.19×10^7 2.33×10^9	5 14	3.28×10^6 7.94×10^7	0.032	3.1	11.1	13 37	4.78×10^7 1.14×10^9	4 12	2.00×10^6 4.51×10^7
9	0.031	3.1	11.1	14 47	8.25×10^7 3.16×10^9	4 12	2.86×10^6 6.28×10^7	0.033	3.3	11.5	12 35	5.93×10^7 1.28×10^9	4 11	2.07×10^6 5.03×10^7

Eq. (19), a and b also correspond to the operation point. The reason for choosing the operation point away from the threshold is as follows. It is known empirically that $p_L \propto (p_Z/p_{Z,\text{th}})^{(d+1)/2}$ when the *minimum weight perfect matching* decoder is used [69]. If we operate closer to the threshold, a larger d is essential to reach some prechosen p_L^{targ} . Thus, the operation point is chosen away from the threshold. Also, sufficiently away from the threshold point the ratio a/b is reasonably constant and the estimation with Eq. (19) is reliable [56]. Once d for achieving p_L^{targ} is determined, \mathcal{N} can be estimated by counting the average number of GHZ states required to build $|\mathcal{C}\rangle_{\mathcal{L}}$ of side $l = 5d/4$. Only the central qubit of a $|\mathcal{C}_*\rangle$ stays in the lattice and the rest of them are consumed by the n -BSMs. A $|\mathcal{C}\rangle_{\mathcal{L}}$ of sides l would have $6l^3$ qubits. Therefore, we need $6l^3 |\mathcal{C}_*\rangle$ states per fault-tolerant gate operation.

As explained in Sec. II C, to create a $|\mathcal{C}_*\rangle$, we need two $|\mathcal{C}_3\rangle_{n,n,n}$ states and one $|\mathcal{C}_3'\rangle_{n,m,n}$ state. Based on the noise model in Sec. III, in order to minimize dephasing effects on the central qubit, we set $m = 2$. According to Fig. 2, the creation of a $|\mathcal{C}_3\rangle_{n,n,n}$ necessitates the entanglement of two $|\text{GHZ}_{n+1}\rangle$ states and a $|\text{GHZ}_{n+2}\rangle$ state using two B_S 's. As the failure rate of one B_S is $(1 + 2\eta)/2$ given a photon-loss rate η [obtained by setting $n = 1$ in Eq. (8)], one needs $8(1 - 2\eta)^{-2}$ copies of $|\text{GHZ}_{n+1}\rangle$ and $4(1 - 2\eta)^{-2}$ copies of $|\text{GHZ}_{n+2}\rangle$, on average. Similarly, to create a $|\mathcal{C}_3'\rangle_{n,m,n}$,

one needs on average $8(1 - 2\eta)^{-2} |\text{GHZ}_{n+1}\rangle$ and $4(1 - 2\eta)^{-2} |\text{GHZ}_{m+2}\rangle$. Therefore,

$$\mathcal{N}_* = \frac{4(6N_{n+1} + 2N_{n+2} + N_{m+2})}{(1 - 2\eta)^2} \quad (20)$$

$|\text{GHZ}_3\rangle$ states consumed to create a $|\mathcal{C}_*\rangle$ in MTQC-1, on average, where N_r is the average number of $|\text{GHZ}_3\rangle$ states consumed to create a $|\text{GHZ}_r\rangle$, example values of which can be read from Table II in Appendix B. On the other hand, one needs

$$\mathcal{N}'_* = \frac{4(6N_{n+1} + 2N_{n+2} + N_{m+2})}{(1 - 2\eta)^2(1 - p_f)^2} \quad (21)$$

$|\text{GHZ}_3\rangle$ states, on average, in MTQC-2. For example, consider the case when $n = 8$ and $m = 2$, and MTQC is operated at $\eta = 0.01$. Looking at Table II in Appendix B and inserting the values of N_{10} , N_9 , and N_4 into Eq. (20) one can estimate that $4(6 \times 55.16 + 2 \times 68.00 + 4.08)(1 - 2 \times 0.01)^{-2} \approx 1962$ $|\text{GHZ}_3\rangle$ states, on average, are consumed in MTQC-1 to create a $|\mathcal{C}_*\rangle$. Similarly, using Eq. (21), we estimate that approximately 1980 $|\text{GHZ}_3\rangle$ states are needed in MTQC-2.

Once the average number of $|\text{GHZ}_3\rangle$ states required to create a $|\mathcal{C}_*\rangle$ is known, it is straightforward to calculate the

resource overhead $\mathcal{N}_{p_L}^{\text{targ}}$ to achieve some p_L^{targ} . In the case of MTQC-1, we have

$$\mathcal{N}_{p_L}^{\text{targ}} = \frac{375(6N_{n+1} + 2N_{n+2} + N_{m+2})}{8(1-2\eta)^2} d^3, \quad (22)$$

and, for MTQC-2, it is

$$\mathcal{N}_{p_L}^{\text{targ}} = \frac{375(6N_{n+1} + 2N_{n+2} + N_{m+2})}{8(1-2\eta)^2(1-p_f)^2} d^3. \quad (23)$$

Let us consider the same example when $n = 8$ and $m = 2$ with a similar value for η to estimate resource overheads. Furthermore, from the simulation results we estimate that one needs $d \approx 15$ (13) to attain $p_L \sim 10^{-6}$ in MTQC-1 (MTQC-2). Using the values of d in Eqs. (22) and (23), we estimate that $\mathcal{N}_{10^{-6}} \approx 8.19 \times 10^7$ and $\mathcal{N}'_{10^{-6}} \approx 4.78 \times 10^7$. On the other hand, for $p_L \sim 10^{-15}$, one needs $d \approx 47$ (37) and thus $\mathcal{N}_{10^{-15}} \approx 2.33 \times 10^9$ and $\mathcal{N}'_{10^{-15}} \approx 1.14 \times 10^9$. Resource overheads and d for other values of n are presented in Table I.

In encoding the qubits of $|\mathcal{C}\rangle_{\mathcal{L}}$ with the three-qubit repetition QEC code, $|\mathcal{C}_{3'}\rangle_{n,m,n}$ is replaced by $|\mathcal{C}_{3'}\rangle_{\text{enc}}$, which is created by replacing $|\text{GHZ}_{m+2}\rangle$ in Fig. 2 by

$$\begin{aligned} |\text{enc}\rangle &= |\text{H}\rangle(|\text{H}\rangle^{\otimes m} + |\text{V}\rangle^{\otimes m})^{\otimes 3} |\text{H}\rangle \\ &+ |\text{V}\rangle(|\text{H}\rangle^{\otimes m} - |\text{V}\rangle^{\otimes m})^{\otimes 3} |\text{V}\rangle. \end{aligned} \quad (24)$$

The process to create $|\text{enc}\rangle$ is detailed in Appendix C. To estimate the resource overhead due to encoding, we first estimate the average number of $|\text{GHZ}_3\rangle$ states consumed to generate $|\text{enc}\rangle$. For this, a $|\text{GHZ}_3\rangle$ and a $|\text{GHZ}_5\rangle$ are needed in the first step (see Appendix C) and are entangled using B_S . When $\eta = 0.01$, $N_{\text{enc}} \approx 104.96$ $|\text{GHZ}_3\rangle$ states are incurred, on average, to form a $|\text{enc}\rangle$ (deduced in Appendix C). Hereafter, the procedure to estimate the resource overhead remains the same as the nonencoded case. Therefore, the resource overheads in the encoded case are

$$\mathcal{N}_{p_L}^{\text{enc}} \Big|_{m=2} = \frac{375(6N_{n+1} + 2N_{n+2} + N_{\text{enc}})}{8(1-2\eta)^2} d^3 \quad (25)$$

for MTQC-1 and

$$\mathcal{N}'_{p_L}^{\text{enc}} \Big|_{m=2} = \frac{375(6N_{n+1} + 2N_{n+2} + N_{\text{enc}})}{8(1-2\eta)^2(1-p_f)^2} d^3 \quad (26)$$

for MTQC-2.

Let us reestimate the resource overhead for the same example case with $n = 8$, $m = 2$, and $\eta = 0.01$ with lattice qubits being encoded. As the encoded MTQC operating under a similar photon-loss condition gives rise to smaller dephasing, that is, $p_{\text{eff}} < p_Z$, smaller d values

suffice to attain p_L^{targ} . The same is reflected in the simulation results. Now, from the simulation we estimate that $d \approx 5$ (4) is essential to attain $p_L \sim 10^{-6}$ in MTQC-1 (MTQC-2). Inserting the values of N_{10} , N_9 , N_{enc} , and η into Eq. (25) one can estimate that $\mathcal{N}_{10^{-6}}^{\text{enc}} \approx 3.28 \times 10^6$ and $\mathcal{N}'_{10^{-6}}^{\text{enc}} \approx 2.0 \times 10^6$. Similarly, to attain $p_L \sim 10^{-15}$, one needs $d \approx 14$ (12). Therefore, $\mathcal{N}_{10^{-15}}^{\text{enc}} \approx 7.94 \times 10^7$ and $\mathcal{N}'_{10^{-15}}^{\text{enc}} \approx 4.41 \times 10^7$. Resource overheads and d in the encoded case for other values of n are presented in Table I

VII. COMPARISON

Now, we compare the performance of our MTQC to other schemes for fault-tolerant linear optical quantum computing. In Fig. 6, we present (a) photon-loss thresholds and (b) resource overheads of known linear optical quantum computing schemes [13, 17, 22, 27–29, 40–42] with MTQC-1 and MTQC-2. Clearly, MTQC shows exceptionally high loss tolerance compared to all known schemes, and is also highly competitive in terms of resource efficiency. In the following we briefly describe each scheme to which MTQC is compared.

The work of Dawson *et al.* [13] was one of the first works to determine the region of η_{th} along with a dephasing error rate and an estimation of resource overheads for fault-tolerant linear optical quantum computing. The scheme uses optical cluster states built using polarization Bell pairs. This scheme couples seven-qubit Steane QEC codes [9] with telecorrection (where teleportation is used for error-syndrome extraction) for fault tolerance. Unlike schemes that use topological codes, the concatenation of Calderbank-Shor-Steane (CSS) codes with itself is employed to attain smaller values of p_L . For example, four (six) levels of concatenation were employed to achieve $p_L \sim 10^{-6}$ (10^{-15}). When $\eta = 4 \times 10^{-3}$ and the depolarization rate is 4×10^{-3} , one has $\mathcal{N}_{10^{-6}} \approx 2.6 \times 10^{19}$ and $\mathcal{N}_{10^{-15}} \approx 7.1 \times 10^{24}$. The resource overhead demanded by the scheme is too high for practical considerations. A subsequent scheme in Ref. [40] that encodes multiple polarization photons into a logical qubit in a *parity state* provides a smaller $\eta_{\text{th}} \approx 2 \times 10^{-3}$, but an improved resource efficiency compared to Ref. [13]. This scheme also uses seven-qubit Steane QEC codes with telecorrection and multiple levels of concatenations. When $\eta = 4 \times 10^{-3}$ and the depolarization rate is 4×10^{-3} , the average number of Bell pairs consumed is $\mathcal{N}_{10^{-6}} \approx 6.8 \times 10^{14}$ and $\mathcal{N}_{10^{-15}} \approx 3.5 \times 10^{19}$ [29] with four and six levels of concatenation, respectively.

Later, Cho [42] used *error-detecting quantum state transfer* where the underlying codes were capable of detecting errors in a way similar to the scheme in Ref. [70]. Here, QEC is done by concatenating different error-detecting codes. This scheme offers a smaller $\eta_{\text{th}} \approx 1.57 \times 10^{-3}$, but the value of N could be reduced by many

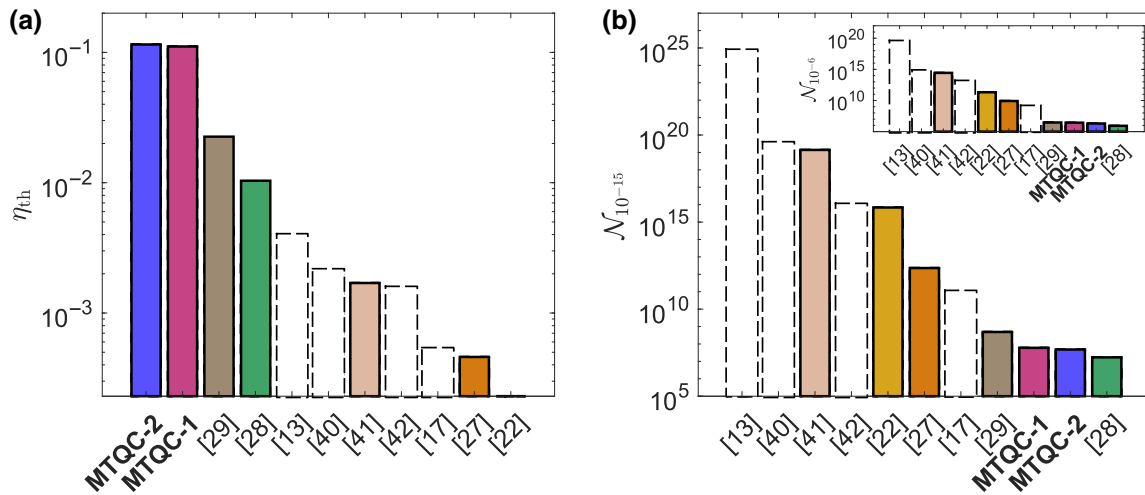


FIG. 6. Contrast of the MTQC-1 and MTQC-2 paradigms, concatenated with repetition codes, against several other reported linear optical quantum computing schemes. (a) In terms of the photon-loss threshold η_{th} , we note that both MTQC-1 and MTQC-2 permit an overall tolerance value that is conspicuously larger than those offered in Refs. [13,40–42] by at least an order of magnitude and those offered in Refs. [17,22,27] by at least 2 orders of magnitude. The η_{th} shown here for the schemes in Refs. [28,29] are at least 3 times as large as the originally published values. This is because, here, we quote the *overall* threshold values for a fair comparison with other schemes; original articles presented componentwise values. It should also be noted that the η_{th} of schemes from Refs. [13,17,40,42], represented by open bars with dashed borders, are valid only for a zero depolarizing error, which is physically unachievable; their loss thresholds under realistic levels of depolarizing (or dephasing) errors must be much lower than the presented values. (b) Both MTQC schemes also excel in terms of resource overheads required to reach a target logical error rate $\mathcal{N}_{10^{-15}}^{\text{target}}$. The inset chart corresponds to $\mathcal{N}_{10^{-6}}^{\text{target}}$, while the main chart corresponds to $\mathcal{N}_{10^{-15}}^{\text{target}}$. It is apparent that MTQC is more efficient in $\mathcal{N}_{10^{-15}}^{\text{target}}$ than other schemes (other than that in Ref. [28]) by several orders of magnitude. Importantly, MTQC ranks almost comparably with the scheme in Ref. [28] as the most resource-efficient schemes known.

orders of magnitude compared to Ref. [13]. When $\eta = 1 \times 10^{-4}$ and the depolarizing rate is 1×10^{-5} , with five (seven) levels of concatenation, the average number of Bell pairs used is $\mathcal{N}_{10^{-6}} \approx O(10^{13})$ [$\mathcal{N}_{10^{-15}} \approx O(10^{16})$]. There is yet another multi-polarization-photon qubit quantum computing scheme [41] that again utilizes telecorrection based on seven-qubit Steane QEC codes and thus needs the same levels of concatenation. Calculations in Ref. [28] show that $\mathcal{N}_{10^{-6}} \approx O(10^{13})$ [$\mathcal{N}_{10^{-15}} \approx O(10^{16})$] Bell pairs are consumed when $\eta \approx O(10^{-4})$ and $p_Z \approx O(10^{-4})$.

Using streams of entangled polarization photons, a topological photonic quantum computing scheme, which involves creating $|\mathcal{C}_{\mathcal{L}}\rangle$, was proposed in Ref. [17]. This has $\eta_{\text{th}} \approx 5.3 \times 10^{-4}$ when the depolarizing error rate is zero. However, this scheme gives $p_{\text{th}} = 1.14 \times 10^{-3}$ for the hypothetical case of $\eta = 0$, which is higher by an order of magnitude compared to other nontopological fault-tolerant architectures. Calculations in Ref. [28] show that $\mathcal{N}_{10^{-6}} > 2 \times 10^9$ ($\mathcal{N}_{10^{-15}} > 4.2 \times 10^{10}$) for nonzero η .

The coherent states $\{|\alpha\rangle, |-\alpha\rangle\}$ can be used as the logical basis for CV qubits [20,22,71]. Lund *et al.* [22] used these qubits to develop a fault-tolerant quantum computing scheme. This also employs seven-qubit Steane QEC codes with telecorrection and multiple levels of concatenations for tolerance against photon loss

and dephasing errors. Here, superpositions of coherent states, $|\alpha\rangle \pm |-\alpha\rangle$ (up to normalization) [72,73], are considered as resources. For this scheme, $\eta_{\text{th}} \approx 2.3 \times 10^{-4}$ and $\mathcal{N}_{10^{-6}} \approx 2.1 \times 10^{11}$ ($\mathcal{N}_{10^{-15}} \approx 6.9 \times 10^{15}$) when $\eta = 8 \times 10^{-5}$ and $p_Z = 2 \times 10^{-4}$. The resource overhead is reduced by many orders of magnitude compared to Ref. [13], but this comes at the cost of a very low η_{th} . Lee and Jeong [27] improved this situation by replacing coherent superposition states with hybrid states. The new scheme offers a better value of $\eta_{\text{th}} \approx 4.6 \times 10^{-4}$. Here $\mathcal{N}_{10^{-6}} \approx 8.2 \times 10^9$ ($\mathcal{N}_{10^{-15}} \approx 2.3 \times 10^{12}$) hybrid qubits are required when $\eta = O(10^{-4})$ and $p_Z = O(10^{-4})$.

Omkar *et al.* [28] showed by far the best η_{th} -to-resource-overhead ratio that is achievable by creating $|\mathcal{C}_{\mathcal{L}}\rangle$ states with hybrid qubits. In the scheme of Ref. [28], $\eta_{\text{th}} \approx 3.3 \times 10^{-3}$ and $\mathcal{N}_{10^{-6}} \approx 8.5 \times 10^5$ ($\mathcal{N}_{10^{-15}} \approx 1.7 \times 10^7$) hybrid qubits are consumed when $\eta = 1.5 \times 10^{-3}$ and $p_Z = 3 \times 10^{-3}$. Subsequently, Omkar *et al.* [29] demonstrated that η_{th} can be further improved by spending more hybrid qubits. This scheme could achieve an improved $\eta_{\text{th}} \approx 5.7 \times 10^{-3}$ with $\mathcal{N}_{10^{-6}} \approx 2.9 \times 10^7$ ($\mathcal{N}_{10^{-15}} \approx 4.9 \times 10^8$) when $\eta = 2.6 \times 10^{-3}$ and $p_Z = 2.3 \times 10^{-3}$.

After the previous overview of various existing linear optical schemes for fault-tolerant quantum computing and mentioning the associated numerical values of η_{th}

and $\mathcal{N}_{p_L}^{\text{targ}}$, we are now set for a comparison with MTQC. We compare with schemes that involve the creation of RHG lattices—the schemes in Refs. [17,28,29]. In comparison, MTQC outperforms the scheme in Ref. [17] both in terms of photon-loss tolerance and resource efficiency. Although the MTQC performs better than schemes in Refs. [28,29] in terms of η_{th} , it falls short in terms of $\mathcal{N}_{p_L}^{\text{targ}}$ compared to the scheme in Ref. [28]. On the other hand, the MTQC outperforms all the known nontopological schemes [13,17,22,27,40–42] both in terms of η_{th} and resource efficiency.

We note that the error models in Refs. [13,17,40,42] employed photon loss and depolarizing errors independently. On the other hand, the other schemes [22,27–29,41] considered more realistic models where photon loss and dephasing are related. In addition, the photon-loss thresholds in Refs. [13,17,40,42] are obtained under the condition of zero depolarizing error, which is unrealistic. For these four schemes, when a nonzero depolarizing error is considered, the threshold values should then be lower than those presented as open bars in Fig. 6(a), since additional depolarizing errors deteriorate η_{th} .

A very recent scheme [74] that also encodes lattice qubits with QEC codes claims to be able to tolerate a photon-loss rate of 10.4% occurring in entangling operations. This requires a particular type of 24-photon entangled states of which information concerning their (unreported) generation resource overheads could be of interest. On the contrary, for MTQC in this work, we begin with only three-photon GHZ states that can be deterministically generated using current technology [37].

The scheme in Ref. [18] considers detectors as resources, about $O(10^9)$ of them, to create a tree cluster state, a collection of which ultimately forms a lattice (similar to the fate of the $|C_*\rangle$). This can tolerate, componentwise, a photon-loss rate of approximately 1×10^{-3} (when the beam splitters are assumed to be lossless and the success rate of a BSM is 0.5). In our work, when $n = 9$, we need 2935 $|GHZ_3\rangle$ states (encoded case) to be consumed, and this number also reflects the order of magnitude of detectors needed. Additionally, our protocol has componentwise $\eta_{\text{th}}^{\text{enc}} \approx 3.7 \times 10^{-2}$, which is a significant improvement. The extravagant resource overhead originates from the usage of single photons as basic ingredients for forming $|GHZ_3\rangle$ states (which are in turn used to generate tree cluster states) with a low success rate of $1/32$ [54]. However, recent work has demonstrated that the success rate can be greater than $1/32$ [75].

VIII. ALTERNATIVE PLATFORMS FOR SCALABILITY ENHANCEMENT

While fault-tolerant MTQC can significantly improve resource overheads and error thresholds relative to other

schemes, it requires resource-state generation and moderately large collective BSMs that could pose a challenge with current polarization-based optical platforms. In particular, repeat-until-success strategies based on polarization-encoded qubits, as discussed in this work and many of the cited references, rely on repeated generation of resource states that involve a huge number of entangled multiphoton qubits.

The use of time-bin qubits (photons encoded into time-delayed pulses of well-separated arrival times that do not overlap one another [76]), which are alternative quantum-information encoding schemes, have been considered in the generation of multiphoton entangled states [77,78]. In particular, it has been shown that such an encoding allows for a deterministic generation of GHZ states [37]. In Ref. [37], specifically, $|C_{3'}\rangle_{n,m,n}$ of $2n + m = 3$ and 4 were generated with respective fidelities of 0.90 and 0.82. Improvement in the fidelity of larger time-bin GHZ states in order to generate $|C_{3'}\rangle_{n,m,n}$ with $m \geq 2$ and $n \geq 8$, which are optimal ranges for MTQC as shown in Table I, is an important research direction.

In the grander scheme of things, it might be of interest to consider the generation of both $|C_3\rangle_{n,n,n}$ and $|C_{3'}\rangle_{n,m,n}$ resource states using the full potential of temporal-mode (TM) optical qubits with both time and frequency content [79–83], where each mode possesses an infinite-dimensional Hilbert space that is encoded onto one physical qubit. By exploiting such a large number of degrees of freedom, it is, in principle, possible to encode multiqubit quantum information onto a single physical photon.

Let us briefly highlight how such a logical TM encoding works. The central operation is the (unitary) quantum pulse gate (QPG) [79,84–86], i.e.,

$$\begin{aligned} \mathcal{Q}_k^{(\theta)} = & 1 - |A_k\rangle\langle A_k| - |C\rangle\langle C| + \cos\theta(|A_k\rangle\langle A_k| + |C\rangle\langle C|) \\ & + \sin\theta(|C\rangle\langle A_k| - |A_k\rangle\langle C|), \end{aligned} \quad (27)$$

which allows one to convert a mode-matched TM basis ket $|A_k\rangle$ ($\langle A_k|A_{k'}\rangle = \delta_{k,k'}$) into the superposition $|A_k\rangle \cos\theta + |C\rangle \sin\theta$, where $|C\rangle$ is a TM in a different frequency band than $|A_k\rangle$ such that $\langle A_k|C\rangle = 0$. On the other hand, a mode-mismatched action, $\mathcal{Q}_k^{(\theta)}|A_{k' \neq k}\rangle = |A_{k'}\rangle$, leaves the TM basis ket intact.

To present an alternative approach to multiqubit cluster-state generation, just as an example, we revisit the so-called type-I fusion scheme [87] that was first introduced to entangle two spatial photons using a PBS, followed by a photodetection after a 45° polarization rotation. If we now suppose that $|A_0\rangle_a$ logically represents $|0_n 0_m 0_n\rangle$ for qubit a and $|A_1\rangle_b$ logically represents $|1_n 1_m 1_n\rangle$ for qubit b , then it has already been shown in Ref. [79] that a QPG-adapted type-I fusion together with a deterministic spatial-mode combination (implicitly carried out throughout this analysis) permits the generation of $|C_{3'}\rangle_a \equiv$

$(|A_0\rangle_a + |A_1\rangle_a)/\sqrt{2}$:

$$|A_0\rangle_a |A_1\rangle_b \xrightarrow{Q_{0,a}^{(\pi/4)} Q_{1,b}^{(\pi/4)}} (|A_0\rangle_a + |C\rangle_a)(|A_1\rangle_b + |C\rangle_b) \frac{1}{2}$$

$$\xrightarrow[\text{single-photon heralding}]{50:50 \text{ beam splitter on } C \text{ modes}} |\mathcal{C}_{3'}\rangle_a. \quad (28)$$

Here, single-photon heralding is performed consistently on *one* of the two output detectors in order to fix all relative phase factors in the final output pure state. One may similarly continue the above type-I fusion procedure until four logical TM basis kets are superposed, resulting in the formation of $|\mathcal{C}_3\rangle_a \equiv (|A'_0\rangle_a + |A'_1\rangle_a + |A'_2\rangle_a - |A'_3\rangle_a)/2$. If $|\psi_M\rangle = \sum_{l=0}^{M-1} |A'_l\rangle/\sqrt{M}$ then

$$|\psi_2\rangle |A'_2\rangle_a \xrightarrow{Q_{1,a}^{(-\pi/2)} Q_{0,a}^{(\pi/4)}} (|\psi_2\rangle_a - |C'\rangle_a) \frac{1}{\sqrt{2}} \otimes |A'_2\rangle_b$$

$$+ |C'\rangle_b \sqrt{2} \frac{1}{\sqrt{3}}$$

$$\xrightarrow[\text{single-photon heralding}]{50:50 \text{ beam splitter on } C' \text{ modes}} |\psi_3\rangle \quad (29)$$

and, finally,

$$|\psi_3\rangle_a |A'_3\rangle_b \xrightarrow{Q_{2,a}^{(-\pi/12)} Q_{1,a}^{(-\pi/2)} Q_{0,a}^{(\pi/4)}} (|\psi_3\rangle_a$$

$$- |C'\rangle_a) \frac{1}{\sqrt{2}} \otimes (|A'_3\rangle_b + |C'\rangle_b \sqrt{3}) \frac{1}{2}$$

$$\xrightarrow[\text{single-photon heralding}]{50:50 \text{ beam splitter on } C' \text{ modes}} |\mathcal{C}_3\rangle_a. \quad (30)$$

Ideally, near-perfect TM manipulation such as the above exemplifying scheme could reduce the average number of photon-pair operations (PPOs) needed to generate resource states, since only two photons are handled at any round of the TM type-I fusion process *via* a 50:50 beam splitter on the C or C' modes followed by detector-specific single-photon heralding. In practical scenarios, reducing the number of PPOs is equivalent to minimizing the number of detectors needed in a scheme as both scale commensurately with each other. As a basic comparison under ideal nonlossy conditions ($\eta = 1$), and hence a 50% chance of a BSM failure, we recall from Sec. VI and Fig. 2 that two GHZ_{n+1} states and one GHZ_{m+2} state are entangled *via* two BSMs to create a copy of $|\mathcal{C}_{3'}\rangle_{n,m,n}$ with polarization encoding. If we suppose that $m = 2$ and $n = 8$ are the target indices then, from Appendix B and the fact that the average number of PPOs needed to create two states and entangle them, given that these states were previously generated with the respective average number of PPOs l_1 and l_2 , is $2(l_1 + l_2 + 1)$ in view of the 0.5 BSM failure

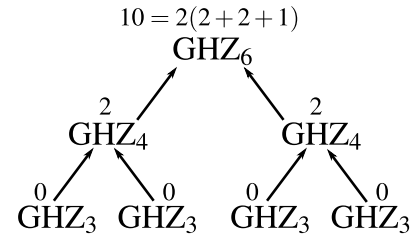


FIG. 7. Counting the average number of PPOs to generate a GHZ_6 state from GHZ_3 states, labeled for every component state.

rate, we require an average of two PPOs (*via* BSMs) to create a GHZ_4 state and 34 PPOs to create a GHZ_9 state. These numbers are obtained from the assumption that no PPOs are required to generate the basic GHZ_3 states (see Fig. 7 for a simple exposition). Therefore, an average of 218 PPOs are necessary to create a copy of $|\mathcal{C}_{3'}\rangle_{8,2,8}$. On the other hand, according to Eq. (28), TM-adapted type-I fusions only require four PPOs on average to create any $|\mathcal{C}_{3'}\rangle_{n,m,n}$ since the success probability of beam-split single-photon heralding on a specified detector is 0.25. Similarly, to create a copy of $|\mathcal{C}_3\rangle_{n,n,n}$, two GHZ_{n+1} states and one GHZ_{n+2} state are entangled. Repeating the above exercise, we find that a total of 378 PPOs are necessary to create $|\mathcal{C}_3\rangle_{8,8,8}$ using polarization encoding, whereas 64 PPOs with TMs [based on Eqs. (28)–(30)] are sufficient to create any $|\mathcal{C}_3\rangle_{n,n,n}$.

The above comparison serves only to give a flavor of what TM encodings can do in terms of reducing the number of PPOs or detectors involved in resource-state generation. More accurate resource-overhead calculations are only available when detailed noise models and QPG

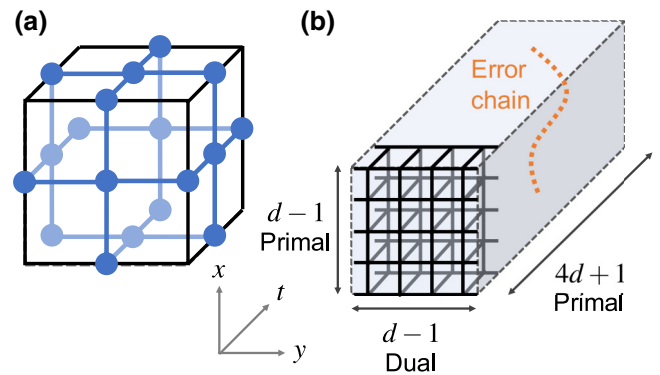


FIG. 8. (a) Primal unit cell of a RHG lattice. Blue dots and lines indicate qubits and edges, respectively. (b) RHG lattice used for the simulation. The lattice is in a cuboid-shaped space of size $d - 1$, $d - 1$, and $4d + 1$ along the x , y , and t (simulating time) axes, respectively, in the unit of a cell. The first primal cells along the t axis are shown as black solid lines. The boundaries are primal about the x and t axes, and dual about the y axis. An error chain connecting the two opposite x or y boundaries (orange dotted line) incurs a logical error.

mechanisms enter the analyses, requiring studies that are beyond the scope of this work. We remind the reader that the above arguments are physically relevant *provided that* orthogonal multiqubit information can be encoded into higher-order orthogonal TMs with high fidelity. However, realistic limitations on the bandwidth, photon-loss tolerance, TM shape switching speed, and other imperfections that affect the QPG’s output fidelity are the primary obstacles that prevent the generation of large superpositions at this stage. Additionally, appropriate error models affecting these TM states require careful and systematic analyses, together with the development of decoders suitable for this optical platform, which are crucial steps that will be reserved for future studies. So, while the existing literature did pave the way for TM quantum computation, much more work is needed in order for practical applications to come to fruition.

IX. DISCUSSION AND CONCLUSION

This work is motivated by recent advancements at the experimental front in the generation of deterministic multiphoton (polarization) entangled states like GHZ states [37]. Here, we described an all-optical protocol that processes multiphoton GHZ states from deterministic sources using only passive linear-optical elements like beam splitters, delay lines, optical switches, and only on-off detectors (no need for photon-number resolution) to build a RHG lattice for fault-tolerant quantum computing. A major shortcoming of using polarization photons, the probabilistic entangling operation, is overcome by first creating multiphoton resource states and then performing n -Bell-state measurements that are near deterministic. However, the multiphoton resource states are created by entangling the three-photon GHZ states using probabilistic direct Bell-state measurements.

With photon loss being a major source of errors, we demonstrated that our protocol offers, without any quantum error-correcting code concatenation, the highest photon threshold of 3.1% in MTQC-1 and 3.3% in MTQC-2. Furthermore, the photon-loss threshold is improved by encoding the lattice qubits in a three-qubit repetition code. This concatenation improves the threshold to 11.1% in MTQC-1 and to 11.5% in MTQC-2. We stress that this drastic improvement is made only with three-photon GHZ states, passive linear-optical elements, and on-off detectors. We also demonstrated that, by employing codes of larger repetition number for concatenation, the photon-loss threshold can be further improved. Furthermore, resource overheads in terms of the average number of three-photon GHZ states incurred per gate operation corresponding to various values of n are tabulated in Table I. In MTQC-2, when $n = 9$, the resource overhead to reach the target logical error rate of 10^{-6} (10^{-15}) is 2.07×10^6 (5.03×10^7).

This is the most resource efficient case of MTQC. Interestingly, we observed that code concatenation not only improves the photon-loss threshold but also favorably reduces the resource overheads of the MTQC. Comparing our results with known linear optical quantum computing schemes [13,17,22,27–29,40–42], MTQC clearly offers the highest tolerance against photon loss. MTQC is also highly resource efficient compared with known linear optical schemes and is comparable only with Ref. [28]. In principle, our protocol can be carried out even if we start with single photons as the basic ingredient. For this, the three-photon GHZ states can be generated using linear optics with a success rate of $1/32$ [54], or higher [75]. In this case, the resource overhead (average number of single photons) for MTQC would increase by approximately 2 orders of magnitude.

In the current work we have not used photon-number-resolving detectors at any stage of the protocol, which is essential to boost the success rate of direct BSM. The reason for this choice is that the on-off detectors are practically more efficient and can operate at room temperatures. If one chooses to employ photon-number-resolving detectors and operate at cryogenic temperatures, the resource efficiency of MTQC can be further improved.

Our protocol can also be extended to the creation of lattices with different geometries [88,89]. However, it remains to be examined if they can be made tolerant against entangling operation failures. MTQC also demonstrates the crucial need for the experimental development of high-fidelity deterministic multiphoton entangled state generators in order for the advancement of the field of scalable linear-optics-based quantum information processing. Given its significant enhancement in the photon-loss threshold and the recent progress in generating multiphoton entanglement, our scheme moves scalable photonic quantum computing a step closer to reality.

ACKNOWLEDGMENTS

This work is supported by National Research Foundation of Korea (NRF) grants funded by the Korea government (Grants No. NRF-2019M3E4A1080074, No. NRF-2020R1A2C1008609 No. NRF-2020K2A9A1A06102946, No. NRF-2019R1A6A1A10073437, and No. NRF-2022M3E4A1076099) via the Institute of Applied Physics at Seoul National University, and by an Institute of Information & Communications Technology Planning & Evaluation (IITP) grant funded by the Korea government (MSIT) (IITP-2021-2020-0-01606, IITP-2021-0-01059). S.W.L. acknowledges support from the National Research Foundation of Korea (2020M3E4A1079939) and the KIST institutional program (2E31531). We thank Kamil Bradler, Brendan Pankovich, Alex Neville, Jano Gil-Lopez, and Benjamin Brecht for insightful discussions.

APPENDIX A: SIMULATION OF QEC

Here we present the method to obtain the logical error rate p_L numerically for a given subvariant of MTQC (MTQC-1 or MTQC-2), a failure rate of an n -BSM (p_f), a dephasing rate (p_Z), and a code distance (d). We consider a three-dimensional space with the x , y , and *simulating time* (t) axes. We simulate a RHG lattice in a cuboid of size $(d-1, d-1, T)$ for $T := 4d+1$ about the three axes in the unit of a cell, as shown in Fig. 8. The boundaries are primal about the x and t axes (that is, they are in contact with primal cells), while they are dual about the y axis (that is, they cut primal cells in a half).

An isolated dephasing error is detected by two *check operators* adjacent to the qubit. Generally, an *error chain* of dephasing errors is detected by two check operators located at its ends [33,34,57,90]. However, error chains connecting two opposite boundaries are not detectable, since there are no check operators at their ends. If the number of such error chains regarding the $x(y)$ boundaries is odd, a *primal (dual) logical error* occurs. We take account of only primal logical errors in this simulation.

The code distance is determined by the widths about the x and y axes, not the t axis; thus, T can be an arbitrary number. For a fair comparison with different code distances or other computation schemes, we calculate the logical error rate *per unit simulating time*. Here T should be large enough to get a reliable value; thus, we set it to $4d+1$.

We carry out Monte Carlo simulations, each by repeating a sampling cycle sufficiently many times to obtain a desired confidence interval of the logical error rate per unit simulation time. Each cycle is structured as follows. We first prepare the cluster state described above. Because an n -BSM fails with probability p_f , qubits are randomly removed by the method described in Sec. V. Next, we ensure that operators containing the removed qubits are merged with adjacent check operators repeatedly until no missing-qubit sites are left [48]. If a qubit on a boundary is removed, the involved check operator is removed and the boundary is deformed to include the other qubits in the check operator. If the two opposite x boundaries meet due to the deformation, we conclude that a *logical loss* occurs, namely, that the desired computation fails. In this case, we stop the cycle and start the next one immediately. Otherwise, dephasing errors are randomly assigned to the left qubits with probability p_Z . For simplicity, qubits on the t boundaries are assumed to be perfect, namely, they are neither removed nor have errors. This ensures that the t boundaries cause no logical losses or errors. Such an unrealistic assumption has negligible effects if T is large enough.

Next, the outcomes of check operators are calculated, then decoded to deduce errors with Edmonds' minimum-weight perfect matching algorithm [91–93] via Blossom V software [94]. Error chains connecting the two opposite

TABLE II. Possible GHZ states at each step k and the corresponding generation processes are tabulated. Here $+_{B_S}$ stands for the BSM B_S . The average number of $|\text{GHZ}_3\rangle$ states consumed in generation of each GHZ state is also tabulated. The numbers in the brackets in the last column correspond to the average number of $|\text{GHZ}_3\rangle$ states consumed in the presence of photon loss of rate $\eta = 0.01$. The photon loss also reduces the success rate of the BSM to $(1-2\eta)/2$, which in turn increases the average number of $|\text{GHZ}_3\rangle$ states consumed.

k	Possible GHZ states	Creation process	Average number of $ \text{GHZ}_3\rangle$ states
1	$ \text{GHZ}_4\rangle$	$ \text{GHZ}_3\rangle +_{B_S} \text{GHZ}_3\rangle$	4 (4.08)
2	$ \text{GHZ}_5\rangle$	$ \text{GHZ}_4\rangle +_{B_S} \text{GHZ}_3\rangle$	10 (10.37)
	$ \text{GHZ}_6\rangle$	$ \text{GHZ}_4\rangle +_{B_S} \text{GHZ}_4\rangle$	16 (16.66)
3	$ \text{GHZ}_7\rangle$	$ \text{GHZ}_5\rangle +_{B_S} \text{GHZ}_4\rangle$	28 (29.50)
	$ \text{GHZ}_8\rangle$	$ \text{GHZ}_5\rangle +_{B_S} \text{GHZ}_5\rangle$	40 (42.33)
	$ \text{GHZ}_9\rangle$	$ \text{GHZ}_6\rangle +_{B_S} \text{GHZ}_5\rangle$	52 (55.16)
	$ \text{GHZ}_{10}\rangle$	$ \text{GHZ}_6\rangle +_{B_S} \text{GHZ}_6\rangle$	64 (68.00)
4	$ \text{GHZ}_{11}\rangle$	$ \text{GHZ}_7\rangle +_{B_S} \text{GHZ}_6\rangle$	88 (94.19)
	\vdots	\vdots	\vdots
	$ \text{GHZ}_{18}\rangle$	$ \text{GHZ}_{10}\rangle +_{B_S} \text{GHZ}_{10}\rangle$	256 (277.55)

x boundaries are identified by comparing the assigned and decoded errors. We then count the number of distinct simulating times corresponding to the ends of the error chains at the boundary of $x=0$, called *erroneous simulating times*.

After repeating enough cycles, we calculate the logical error rate per unit simulating time p_L by the ratio of the number of erroneous simulating times to the total simulating times. The error threshold p_{th} is obtained from the calculated p_L results for different values of d and p_Z ; p_L decreases as d increases if $p_Z < p_{\text{th}}$, and vice versa otherwise.

APPENDIX B: COUNTING THE $|\text{GHZ}_3\rangle$ STATES TO GENERATE $|\text{GHZ}_r\rangle$

The *average* total number of $|\text{GHZ}_3\rangle$ states required to perform one successful BSM of two GHZ states of sizes m_1 and m_2 is given by $2(N_{m_1} + N_{m_2})$, where N_{m_1} , for instance, is the number of $|\text{GHZ}_3\rangle$ states used to generate $|\text{GHZ}_{m_1}\rangle$, and the factor 2 accounts for the 1/2 success rate of a BSM. Using the shorthand notation $+_{B_S}$, we may define $N_{m=m_1+m_2-2} = N_{m_1} +_{B_S} N_{m_2} \equiv 2(N_{m_1} + N_{m_2})$, where the resulting $|\text{GHZ}_m\rangle$ from this BSM is always two less than the sum of the constituent sizes. The operation $+_{B_S}$ is nonassociative— $A +_{B_S} (B +_{B_S} C) \neq (A +_{B_S} B) +_{B_S} C$.

Based on the above iterative generation protocol, it takes $k = \lceil \log_2(m-2) \rceil$ steps to create a $|\text{GHZ}_m\rangle$ state from a minimal set of $M = m-2$ $|\text{GHZ}_3\rangle$ states. The average numbers of $|\text{GHZ}_3\rangle$ states required to build GHZ states of various sizes are listed in Table II.

According to simple geometric-sum identities, we additionally note that entangling a set of M $|\text{GHZ}_3\rangle$ kets *in*

any fixed sequential order yields the resource requirement $N_M = 3 \cdot 2^{M-1} - 2$. Such a naive way of entangling GHZ-3 states can result in an excessively large N_M . If we define an entangling step as the step in which a maximal number of *independent* BSMs are carried out, then an optimal way of entangling GHZ states is to minimize the number of sequential operations at each step.

Starting with the step counter $k = 1$ and $m - 2$ GHZ-3 states needed to create a $|\text{GHZ}_m\rangle$, an efficient recipe for creating a $|\text{GHZ}_m\rangle$ state from a BSM of $|\text{GHZ}_3\rangle$ states as basic ingredients can be presented in the following iterative scheme.

1. Let M denote the total number of ingredient GHZ states to be entangled using BSMs. When $k = 1$, for example, $M = m - 2$.
2. If M is odd, define the number of GHZ pairs $n_p = (M - 1)/2$ with $n_{\text{left}} = 1$ GHZ ket leftover. Otherwise, define $n_p = M/2$ and $n_{\text{left}} = 1$.
3. Proceed with n_p distinct pairwise BSMs of GHZ states. If M is odd, $n_{\text{left}} = 1$ GHZ state will not be entangled, which will be pairwise entangled with another GHZ state in the next step.
4. If $M = 1$, terminate the generation protocol. Otherwise, update $M = n_p + n_{\text{left}}$ and raise k by one.

Using this numerical recipe, the (unbracketed) values in Table II can be generated. Upon numerical-pattern inspection, we find the explicit analytical formula

$$N_m = 3(m - 2) \cdot 2^{\lfloor \log_2(m-2) \rfloor} - 2 \times 4^{\lfloor \log_2(m-2) \rfloor} \quad (\text{B1})$$

for the number of GHZ_3 states needed to generate a GHZ_m state.

APPENDIX C: GENERATION OF A CONCATENATED RESOURCE STATE

In this section we describe how to create a resource state concatenated with the three-qubit repetition QEC code, that is, $|\mathcal{C}_{3'}\rangle_{\text{enc}} = |0_n\rangle(|0_m\rangle + |1_m\rangle)^{\otimes 3}|0_n\rangle + |1_n\rangle(|0_m\rangle - |1_m\rangle)^{\otimes 3}|1_n\rangle$. This state can be generated in the $[k = \log_2(m - 1)]$ th step when using $|\text{GHZ}_3\rangle$. To begin with, apply the Hadamard operation on $|\text{GHZ}_{m+1}\rangle$ so that we have $H_{m+1}|\text{GHZ}_{m+1}\rangle = (|H\rangle^{\otimes m} + |V\rangle^{\otimes m})|H\rangle + (|H\rangle^{\otimes m} - |V\rangle^{\otimes m})|V\rangle$. Applying B_S between $H_{m+1}|\text{GHZ}_{m+1}\rangle$ and $|\text{GHZ}_5\rangle$, and rearranging the modes, we get $|H\rangle(|H\rangle^{\otimes m} + |V\rangle^{\otimes m})|H\rangle^{\otimes 3} + |V\rangle(|H\rangle^{\otimes m} - |V\rangle^{\otimes m})|V\rangle^{\otimes 3}$ in the $(k + 1)$ th step. Furthermore, by entangling two $H_{m+1}|\text{GHZ}_{m+1}\rangle$ states with the above state, we get the encoded central qubit

$$\begin{aligned} |\text{enc}\rangle = & |H\rangle(|H\rangle^{\otimes m} + |V\rangle^{\otimes m})^{\otimes 3}|H\rangle \\ & + |V\rangle(|H\rangle^{\otimes m} - |V\rangle^{\otimes m})^{\otimes 3}|V\rangle, \end{aligned} \quad (\text{C1})$$

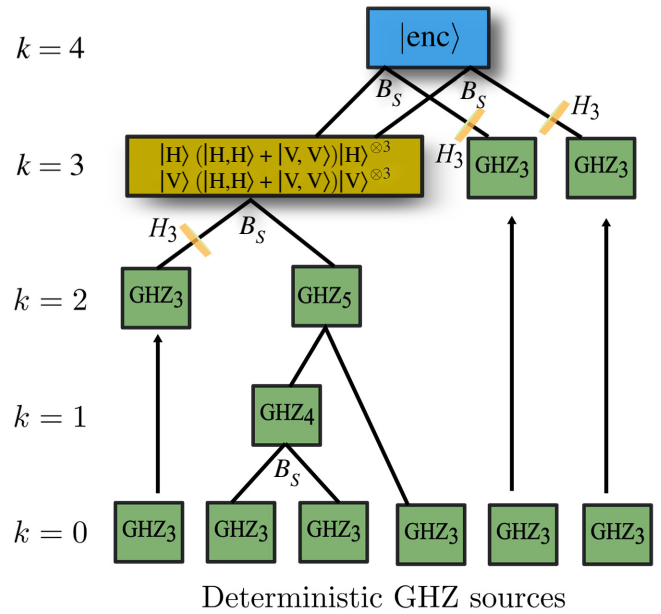


FIG. 9. Schematic representation of the process of generation of $|\text{enc}\rangle$ using $|\text{GHZ}_3\rangle$ states and B_S in $k = 4$ steps. Here H_3 is the Hadamard operation on the third photon of $|\text{GHZ}_3\rangle$ and is performed before feeding it to B_S .

in the $(k + 2)$ th step. Finally, two $|\text{GHZ}_{n+1}\rangle$ states are entangled on both sides of $|\text{enc}\rangle$ to get the desired state $|\mathcal{C}_{3'}\rangle_{\text{enc}}$. This final step is nothing but replacing $|\text{GHZ}_{m+2}\rangle$ with $|\text{enc}\rangle$ in the k th step in Fig. 2. In step $k = 2$, $(1 + 10)/0.5 = 22$ $|\text{GHZ}_3\rangle$ states are consumed on average. Furthermore, $(22 + 2)/(0.5 \times 0.5) = 96$ $|\text{GHZ}_3\rangle$ states are consumed on average in the creation of a $|\text{enc}\rangle$. However, taking in to account the photon loss of rate $\eta = 0.01$, the average number of $|\text{GHZ}_3\rangle$ states consumed in the $(k = 2)$ th step is $(1 + 10.37)/[(1 - 2\eta)/2] = 23.20$ and finally it is $(23.20 + 2)/[(1 - 2\eta)/2]^2 \approx 104.96$. Figure 9 supplements these statements with a flowchart.

When we have $m = 2$, the first process in the creation of $|\text{enc}\rangle$ takes place in $k = 2$ time steps. Therefore, creation of $|\text{enc}\rangle$ takes a total of four steps. In the unencoded case, the central qubit always waited for two time steps during the creation of $|\mathcal{C}_{3'}\rangle$ and a total of $k = 4$ (5) time steps for $|\mathcal{C}_{\mathcal{L}}\rangle$ in MTQC-1 (MTQC-2). In the encoded case the central qubit has to wait for a total of $k = 6$ (7) time steps before being measured for quantum computing.

- [1] P. Kok, W. J. Munro, K. Nemoto, T. C. Ralph, J. P. Dowling, and G. J. Milburn, Linear optical quantum computing with photonic qubits, *Rev. Mod. Phys.* **79**, 135 (2007).
- [2] T. C. Ralph and G. J. Pryde, Chapter 4—optical quantum computation, *Prog. Opt.* **54**, 209 (2010).

- [3] R. Knill, E. Laflamme, and G. J. Milburn, A scheme for efficient quantum computation with linear optics, *Nature* **409**, 46 (2001).
- [4] J. L. O'Brien, Optical quantum computing, *Science* **318**, 1567 (2007).
- [5] R. Raussendorf and H. J. Briegel, A One-Way Quantum Computer, *Phys. Rev. Lett.* **86**, 5188 (2001).
- [6] M. A. Nielsen, Optical Quantum Computation Using Cluster States, *Phys. Rev. Lett.* **93**, 040503 (2004).
- [7] N. Lütkenhaus, J. Calsamiglia, and K.-A. Suominen, Bell measurements for teleportation, *Phys. Rev. A* **59**, 3295 (1999).
- [8] N. F. Tyndall, T. H. Stievater, D. A. Kozak, M. W. Pruessner, W. S. Rabinovich, N. M. Fahrenkopf, A. O. Antohe, and K. A. McComber, in *Smart Photonic and Optoelectronic Integrated Circuits XXIII*, Vol. 11690 (SPIE, 2021), p. 40, <https://spie.org/Publications/Proceedings/Volume/11690?SSO=Inlinear optics and hybrid qubits>
- [9] M. A. Nielsen and I. L. Chuang, *Quantum Computation and Quantum Information* (Cambridge University Press, Cambridge, 2010).
- [10] D. A. Lidar and T. A. Brun, *Quantum Error Correction* (Cambridge University Press, Cambridge, 2013).
- [11] A. M. Steane, Overhead and noise threshold of fault-tolerant quantum error correction, *Phys. Rev. A* **68**, 042322 (2003).
- [12] E. Knill, Quantum computing with realistically noisy devices, *Nature* **434**, 39 (2005).
- [13] C. M. Dawson, H. L. Haselgrove, and M. A. Nielsen, Noise thresholds for optical cluster-state quantum computation, *Phys. Rev. A* **73**, 052306 (2006).
- [14] N. Lütkenhaus and J. Calsamiglia, Maximum efficiency of a linear-optical Bell-state analyzer, *Appl. Phys. B* **72**, 67 (2001).
- [15] Y. Li, S. D. Barrett, T. M. Stace, and S. C. Benjamin, Fault Tolerant Quantum Computation with Nondeterministic Gates, *Phys. Rev. Lett.* **105**, 250502 (2010).
- [16] K. Fujii and Y. Tokunaga, Fault-Tolerant Topological One-Way Quantum Computation with Probabilistic Two-Qubit Gates, *Phys. Rev. Lett.* **105**, 250503 (2010).
- [17] D. A. Herrera-Martí, A. G. Fowler, D. Jennings, and T. Rudolph, Photonic implementation for the topological cluster-state quantum computer, *Phys. Rev. A* **82**, 032332 (2010).
- [18] Y. Li, P. C. Humphreys, G. J. Mendoza, and S. C. Benjamin, Resource costs for fault-tolerant linear optical quantum computing, *Phys. Rev. X* **5**, 041007 (2015).
- [19] D. Bonneau, G. J. Mendoza, J. L. O'Brien, and M. G. Thompson, Effect of loss on multiplexed single-photon sources, *New J. Phys.* **17**, 043057 (2015).
- [20] H. Jeong and M. S. Kim, Efficient quantum computation using coherent states, *Phys. Rev. A* **65**, 042305 (2002).
- [21] T. C. Ralph, A. Gilchrist, G. J. Milburn, W. J. Munro, and S. Glancy, Quantum computation with optical coherent states, *Phys. Rev. A* **68**, 042319 (2003).
- [22] A. P. Lund, T. C. Ralph, and H. L. Haselgrove, Fault-Tolerant Linear Optical Quantum Computing with Small-Amplitude Coherent States, *Phys. Rev. Lett.* **100**, 030503 (2008).
- [23] C. R. Myers and T. C. Ralph, Coherent state topological cluster state production, *New J. Phys.* **13**, 115015 (2011).
- [24] H. Jeong, M. S. Kim, and J. Lee, Quantum-information processing for a coherent superposition state via a mixed-entangled coherent channel, *Phys. Rev. A* **64**, 052308 (2001).
- [25] K. Fukui, A. Tomita, A. Okamoto, and K. Fujii, High-threshold fault-tolerant quantum computation with analog quantum error correction, *Phys. Rev. X* **8**, 021054 (2018).
- [26] I. Tzitrin, T. Matsuura, R. N. Alexander, G. Dauphinais, J. E. Bourassa, K. K. Sabapathy, N. C. Menicucci, and I. Dhand, Fault-Tolerant Quantum Computation with Static Linear Optics, *PRX Quantum* **2**, 040353 (2021).
- [27] S.-W. Lee and H. Jeong, Near-deterministic quantum teleportation and resource-efficient quantum computation using linear optics and hybrid qubits, *Phys. Rev. A* **87**, 022326 (2013).
- [28] S. Omkar, Y. S. Teo, and H. Jeong, Resource-Efficient Topological Fault-Tolerant Quantum Computation with Hybrid Entanglement of Light, *Phys. Rev. Lett.* **125**, 060501 (2020).
- [29] S. Omkar, Y. S. Teo, S.-W. Lee, and H. Jeong, Highly photon-loss-tolerant quantum computing using hybrid qubits, *Phys. Rev. A* **103**, 032602 (2021).
- [30] U. L. Andersen, J. S. Neergaard-Nielsen, P. van Loock, and A. Furusawa, Hybrid discrete- and continuous-variable quantum information, *Nat. Phys.* **11**, 713 (2015).
- [31] S. Takeda, T. Mizuta, M. Fuwa, P. van Loock, and A. Furusawa, Deterministic quantum teleportation of photonic quantum bits by a hybrid technique, *Nature* **500**, 315 (2013).
- [32] S. J. D. Phoenix, Wave-packet evolution in the damped oscillator, *Phys. Rev. A* **41**, 5132 (1990).
- [33] R. Raussendorf, J. Harrington, and K. Goyal, A fault-tolerant one-way quantum computer, *Ann. Phys. (N. Y.)* **321**, 2242 (2006).
- [34] R. Raussendorf, J. Harrington, and K. Goyal, Topological fault-tolerance in cluster state quantum computation, *New J. Phys.* **9**, 199 (2007).
- [35] C. Schön, E. Solano, F. Verstraete, J. I. Cirac, and M. M. Wolf, Sequential Generation of Entangled Multiqubit States, *Phys. Rev. Lett.* **95**, 110503 (2005).
- [36] N. H. Lindner and T. Rudolph, Proposal for Pulsed On-Demand Sources of Photonic Cluster State Strings, *Phys. Rev. Lett.* **103**, 113602 (2009).
- [37] J.-C. Besse, K. Reuer, M. C. Collodo, A. Wulff, L. Wernli, A. Copetudo, D. Malz, P. Magnard, A. Akin, M. Gabureac, G. J. Norris, J. I. Cirac, A. Wallraff, and C. Eichler, Realizing a deterministic source of multipartite-entangled photonic qubits, *Nat. Commun.* **11**, 4877 (2020).
- [38] I. Schwartz, D. Cogan, E. R. Schmidgall, Y. Don, L. Gantz, O. Kenneth, N. H. Lindner, and D. Gershoni, Deterministic generation of a cluster state of entangled photons, *Science* **354**, 434 (2016).
- [39] S. Takeda, K. Takase, and A. Furusawa, On-demand photonic entanglement synthesizer, *Sci. Adv.* **5**, eaaw4530 (2019).

- [40] A. J. F. Hayes, H. L. Haselgrove, A. Gilchrist, and T. C. Ralph, Fault tolerance in parity-state linear optical quantum computing, *Phys. Rev. A* **82**, 022323 (2010).
- [41] S.-W. Lee, K. Park, T. C. Ralph, and H. Jeong, Nearly Deterministic Bell Measurement for Multiphoton Qubits and Its Application to Quantum Information Processing, *Phys. Rev. Lett.* **114**, 113603 (2015).
- [42] J. Cho, Fault-tolerant linear optics quantum computation by error-detecting quantum state transfer, *Phys. Rev. A* **76**, 042311 (2007).
- [43] M. Endo, T. Sonoyama, M. Matsuyama, F. Okamoto, S. Miki, M. Yabuno, F. China, H. Terai, and A. Furusawa, Quantum detector tomography of a superconducting nanostrip photon-number-resolving detector, *Opt. Express* **29**, 11728 (2021).
- [44] R. Nehra, A. Win, M. Eaton, R. Shahrokshahi, N. Sridhar, T. Gerrits, A. Lita, S. W. Nam, and O. Pfister, State-independent quantum state tomography by photon-number-resolving measurements, *Optica* **6**, 1356 (2019).
- [45] L. C. Comandar, B. Fröhlich, M. Lucamarini, K. A. Patel, A. W. Sharpe, J. F. Dynes, Z. L. Yuan, R. V. Penty, and A. J. Shields, Room temperature single-photon detectors for high bit rate quantum key distribution, *Appl. Phys. Lett.* **104**, 021101 (2014).
- [46] W. P. Grice, Arbitrarily complete Bell-state measurement using only linear optical elements, *Phys. Rev. A* **84**, 042331 (2011).
- [47] F. Ewert and P. van Loock, 3/4-Efficient Bell Measurement with Passive Linear Optics and Unentangled Ancillae, *Phys. Rev. Lett.* **113**, 140403 (2014).
- [48] J. M. Auger, H. Anwar, M. Gimeno-Segovia, T. M. Stace, and D. E. Browne, Fault-tolerant quantum computation with nondeterministic entangling gates, *Phys. Rev. A* **97**, 030301 (2018).
- [49] D. Herr, A. Paler, S. J. Devitt, and F. Nori, A local and scalable lattice renormalization method for ballistic quantum computation, *npj Quantum Inf.* **4**, 27 (2018).
- [50] K. Takase, J.-I. Yoshikawa, W. Asavanant, M. Endo, and A. Furusawa, Generation of optical Schrödinger cat states by generalized photon subtraction, *Phys. Rev. A* **103**, 013710 (2021).
- [51] M. V. Larsen, X. Guo, C. R. Breum, J. S. Neergaard-Nielsen, and U. L. Andersen, Deterministic generation of a two-dimensional cluster state, *Science* **366**, 369 (2019).
- [52] W. Asavanant, Y. Shiozawa, S. Yokoyama, B. Charoensombutamon, H. Emura, R. N. Alexander, S. Takeda, J. ichi Yoshikawa, N. C. Menicucci, H. Yonezawa, and A. Furusawa, Generation of time-domain-multiplexed two-dimensional cluster state, *Science* **366**, 373 (2019).
- [53] M. Varnava, D. E. Browne, and T. Rudolph, Loss Tolerance in One-Way Quantum Computation via Counterfactual Error Correction, *Phys. Rev. Lett.* **97**, 120501 (2006).
- [54] M. Varnava, D. E. Browne, and T. Rudolph, How Good Must Single Photon Sources and Detectors be for Efficient Linear Optical Quantum Computation?, *Phys. Rev. Lett.* **100**, 060502 (2008).
- [55] S. D. Barrett and T. M. Stace, Fault Tolerant Quantum Computation with Very High Threshold for Loss Errors, *Phys. Rev. Lett.* **105**, 200502 (2010).
- [56] A. C. Whiteside and A. G. Fowler, Upper bound for loss in practical topological-cluster-state quantum computing, *Phys. Rev. A* **90**, 052316 (2014).
- [57] R. Raussendorf and J. Harrington, Fault-Tolerant Quantum Computation with High Threshold in Two Dimensions, *Phys. Rev. Lett.* **98**, 190504 (2007).
- [58] A. G. Fowler and K. Goyal, Topological cluster state quantum computing, *Quantum Inf. Comput.* **9**, 721 (2009).
- [59] M. Zwerger, B. P. Lanyon, T. E. Northup, C. A. Muschik, W. Dür, and N. Sangouard, Quantum repeaters based on trapped ions with decoherence-free subspace encoding, *Quantum Sci. Technol.* **2**, 044001 (2017).
- [60] S. Omkar, R. Srikanth, and S. Banerjee, Dissipative and non-dissipative single-qubit channels: Dynamics and geometry, *Quantum Inf. Process.* **12**, 3725 (2013).
- [61] S. Omkar, R. Srikanth, and S. Banerjee, The operator-sum-difference representation of a quantum noise channel, *Quantum Inf. Process.* **14**, 2255 (2015).
- [62] R. Srikanth and S. Banerjee, Squeezed generalized amplitude damping channel, *Phys. Rev. A* **77**, 012318 (2008).
- [63] U. Shrikant, R. Srikanth, and S. Banerjee, Non-Markovian dephasing and depolarizing channels, *Phys. Rev. A* **98**, 032328 (2018).
- [64] C. D. Lorenz and R. M. Ziff, Precise determination of the bond percolation thresholds and finite-size scaling corrections for the sc, fcc, and bcc lattices, *Phys. Rev. E* **57**, 230 (1998).
- [65] M. Pant, D. Towsley, D. Englund, and S. Guha, Percolation thresholds for photonic quantum computing, *Nat. Commun.* **10**, 1070 (2019).
- [66] M. Gimeno-Segovia, P. Shadbolt, D. E. Browne, and T. Rudolph, From Three-Photon Greenberger-Horne-Zeilinger States to Ballistic Universal Quantum Computation, *Phys. Rev. Lett.* **115**, 020502 (2015).
- [67] S. Omkar, R. Srikanth, and S. Banerjee, Characterization of quantum dynamics using quantum error correction, *Phys. Rev. A* **91**, 012324 (2015).
- [68] S. Omkar, R. Srikanth, and S. Banerjee, Quantum code for quantum error characterization, *Phys. Rev. A* **91**, 052309 (2015).
- [69] A. G. Fowler, M. Mariantoni, J. M. Martinis, and A. N. Cleland, Surface codes: Towards practical large-scale quantum computation, *Phys. Rev. A* **86**, 032324 (2012).
- [70] E. Knill, Quantum computing with realistically noisy devices, *Nature* **434**, 39 (2005).
- [71] T. C. Ralph, A. Gilchrist, G. J. Milburn, W. J. Munro, and S. Glancy, Quantum computation with optical coherent states, *Phys. Rev. A* **68**, 042319 (2003).
- [72] B. Yurke and D. Stoler, Generating Quantum Mechanical Superpositions of Macroscopically Distinguishable States via Amplitude Dispersion, *Phys. Rev. Lett.* **57**, 13 (1986).
- [73] A. Ourjoumtsev, H. Jeong, R. Tualle-Brouiri, and P. Grangier, Generation of optical “Schrödinger cats” from photon number states, *Nature* **448**, 784 (2007).
- [74] S. Bartolucci, P. Birchall, H. Bombin, H. Cable, C. Dawson, M. Gimeno-Segovia, E. Johnston, K. Kieling, N. Nickerson, M. Pant, F. Pastawski, T. Rudolph, and C. Sparrow, Fusion-based quantum computation, *ArXiv:2101.09310* (2021).

- [75] S. Bartolucci, P. M. Birchall, M. Gimeno-Segovia, E. Johnston, K. Kieling, M. Pant, T. Rudolph, J. Smith, C. Sparrow, and M. D. Vidrighin, Creation of entangled photonic states using linear optics, [ArXiv:2106.13825](https://arxiv.org/abs/2106.13825) (2021).
- [76] C. L. Morrison, F. Graffitti, P. Barrow, A. Pickston, J. Ho, and A. Fedrizzi, Frequency-bin entanglement from domain-engineered down-conversion, *APL Photonics* **7**, 066102 (2022).
- [77] N. C. Menicucci, X. Ma, and T. C. Ralph, Arbitrarily Large Continuous-Variable Cluster States from a Single Quantum Nondemolition Gate, *Phys. Rev. Lett.* **104**, 250503 (2010).
- [78] J. P. Lee, B. Villa, A. J. Bennett, R. M. Stevenson, D. J. P. Ellis, I. Farrer, D. A. Ritchie, and A. J. Shields, A quantum dot as a source of time-bin entangled multi-photon states, *Quantum Sci. Technol.* **4**, 025011 (2019).
- [79] B. Brecht, D. V. Reddy, C. Silberhorn, and M. G. Raymer, Photon temporal modes: A complete framework for quantum information science, *Phys. Rev. X* **5**, 041017 (2015).
- [80] P. C. Humphreys, W. S. Kolthammer, J. Nunn, M. Barbieri, A. Datta, and I. A. Walmsley, Continuous-Variable Quantum Computing in Optical Time-Frequency Modes Using Quantum Memories, *Phys. Rev. Lett.* **113**, 130502 (2014).
- [81] R. N. Alexander, P. Wang, N. Sridhar, M. Chen, O. Pfister, and N. C. Menicucci, One-way quantum computing with arbitrarily large time-frequency continuous-variable cluster states from a single optical parametric oscillator, *Phys. Rev. A* **94**, 032327 (2016).
- [82] P. Roztock, *et al.*, in *2020 22nd International Conference on Transparent Optical Networks (ICTON)* (IEEE, 2020), p. 1, <https://ieeexplore.ieee.org/xpl/conhome/9194588/proceeding>.
- [83] X. Zhu, C.-H. Chang, C. González-Arciniegas, A. Pe'er, J. Higgins, and O. Pfister, Hypercubic cluster states in the phase-modulated quantum optical frequency comb, *Optica* **8**, 281 (2021).
- [84] A. Eckstein, B. Brecht, and C. Silberhorn, A quantum pulse gate based on spectrally engineered sum frequency generation, *Opt. Express* **19**, 13770 (2011).
- [85] B. Brecht, A. Eckstein, A. Christ, H. Suche, and C. Silberhorn, From quantum pulse gate to quantum pulse shaper—engineered frequency conversion in nonlinear optical waveguides, *New J. Phys.* **13**, 065029 (2011).
- [86] J. Gil-Lopez, Y. S. Teo, S. De, B. Brecht, H. Jeong, C. Silberhorn, and L. L. Sánchez-Soto, Universal compressive tomography in the time-frequency domain, *Optica* **8**, 1296 (2021).
- [87] D. E. Browne and T. Rudolph, Resource-Efficient Linear Optical Quantum Computation, *Phys. Rev. Lett.* **95**, 010501 (2005).
- [88] S.-H. Lee and H. Jeong, Universal resource-efficient topological measurement-based quantum computation via color-code-based cluster states, [ArXiv:2106.07530](https://arxiv.org/abs/2106.07530) (2021).
- [89] B. Criger and B. Terhal, Noise thresholds for the $[4, 2, 2]$ -concatenated toric code, *Quantum Inf. Comput.* **16**, 1261 (2016).
- [90] A. G. Fowler and K. Goyal, Topological cluster state quantum computing, *Quantum Info. Comput.* **9**, 721 (2009).
- [91] J. Edmonds, Paths, trees, and flowers, *Can. J. Math.* **17**, 449 (1965).
- [92] J. Edmonds, Maximum matching and a polyhedron with 0, 1-vertices, *J. Res. Nat. Bur. Stand. B* **69**, 55 (1965).
- [93] A. G. Fowler, Minimum weight perfect matching of fault-tolerant topological quantum error correction in average $O(1)$ parallel time, *Quantum Info. Comput.* **15**, 145 (2015).
- [94] V. Kolmogorov, Blossom V: A new implementation of a minimum cost perfect matching algorithm, *Math. Program. Comput.* **1**, 43 (2009).